

## Interactions between the Indonesian Throughflow and circulations in the Indian and Pacific Oceans

Julian P. McCreary<sup>a,\*</sup>, Toru Miyama<sup>b</sup>, Ryo Furue<sup>a</sup>, Tommy Jensen<sup>a</sup>,  
Hyouon-Woo Kang<sup>a,1</sup>, Bohyun Bang<sup>a</sup>, Tangdong Qu<sup>a</sup>

<sup>a</sup> *International Pacific Research Center, University of Hawaii, Honolulu, HI, United States*

<sup>b</sup> *Frontier Research System for Global Change, Yokohama, Japan*

Received 25 October 2006; received in revised form 16 April 2007; accepted 25 May 2007

Available online 6 July 2007

---

### Abstract

Circulations associated with the Indonesian Throughflow (IT), particularly concerning subsurface currents in the Pacific Ocean, are studied using three types of models: a linear, continuously stratified (LCS) model and a nonlinear,  $4\frac{1}{2}$ -layer model (LOM), both confined to the Indo-Pacific basin; and a global, ocean general circulation model (COCO). Solutions are wind forced, and obtained with both open and closed Indonesian passages. Layers 1–4 of LOM correspond to near-surface, thermocline, subthermocline (thermostad), and upper-intermediate (AAIW) water, respectively, and analogous layers are defined for COCO.

The three models share a common dynamics. When the Indonesian passages are abruptly opened, barotropic and baroclinic waves radiate into the interiors of both oceans. The steady-state, barotropic flow field from the difference (open – closed) solution is an anticlockwise circulation around the perimeter of the southern Indian Ocean, with its meridional branches confined to the western boundaries of both oceans. In contrast, steady-state, baroclinic flows extend into the interiors of both basins, a consequence of damping of baroclinic waves by diapycnal processes (internal diffusion, upwelling and subduction, and convective overturning). Deep IT-associated currents are the subsurface parts of these baroclinic flows. In the Pacific, they tend to be directed eastward and poleward, extend throughout the basin, and are closed by upwelling in the eastern ocean and Subpolar Gyre. Smaller-scale aspects of their structure vary significantly among the models, depending on the nature of their diapycnal mixing.

At the exit to the Indonesian Seas, the IT is highly surface trapped in all the models, with a prominent, deep core in the LCS model and in LOM. The separation into two cores is due to near-equatorial, eastward-flowing, subsurface currents in the Pacific Ocean, which drain layer 2 and layer 3 waters from the western ocean to supply water for the upwelling regions in the eastern ocean; indeed, depending on the strength and parameterization of vertical diffusion in the Pacific interior, the draining can be strong enough that layer 3 water flows from the Indian to Pacific Ocean. The IT in COCO lacks a significant deep core, likely because the model's coarse bottom topography has no throughflow passage below 1000 m. Consistent with observations, water in the near-surface (deep) core comes mostly from the northern (southern) hemisphere, a

---

\* Corresponding author. Address: IPRC/SOEST, University of Hawaii, POST Bldg. 401, 1680 East West Road, Honolulu, HI 96822, United States. Tel.: +1 808 956 2216; fax: +1 808 956 9425.

E-mail address: [jay@hawaii.edu](mailto:jay@hawaii.edu) (J.P. McCreary).

<sup>1</sup> Present address: Coastal and Harbor Engineering Laboratory, Korea Ocean Research and Development Institute, Ansan, Republic of Korea.

consequence of the wind-driven circulation in the tropical North Pacific being mostly confined to the upper ocean; as a result, it causes the near-surface current along the New Guinea coast to retroflect eastward, but has little impact on the deeper New Guinea undercurrent.

In the South Pacific, the IT-associated flow into the basin is spread roughly uniformly throughout all four layers, a consequence of downwelling processes in the Indian Ocean. The inflow first circulates around the Subtropical Gyre, and then bends northward at the Australian coast to flow to the equator within the western boundary currents. To allow for this additional, northward transport, the bifurcation latitude of the South Equatorial Current shifts southward when the Indonesian passages are open. The shift is greater at depth (layers 3 and 4), changing from about 14°S when the passages are closed to 19°S when they are open and, hence, accounting for the northward-flowing Great Barrier Reef Undercurrent in that latitude range.

After flowing along the New Guinea coast, most waters in layers 1–3 bend offshore to join the North Equatorial Countercurrent, Equatorial Undercurrent, and southern Tsuchiya Jet, respectively, thereby ensuring that northern hemisphere waters contribute significantly to the IT. In contrast, much of the layer 4 water directly exits the basin via the IT, but some also flows into the subpolar North Pacific. Except for the direct layer 4 outflow, all other IT-associated waters circulate about the North Pacific before they finally enter the Indonesian Seas via the Mindanao Current.

© 2007 Elsevier Ltd. All rights reserved.

*Keywords:* Indonesian Throughflow; Pacific Ocean; Indian Ocean; Antarctic Intermediate Water; Therstodad water; Great Barrier Reef Undercurrent; Tsuchiya Jets

## 1. Introduction

### 1.1. Observations

The Indonesian Seas (Fig. 1) allow primarily warm and fresh, near-surface waters to flow from the Pacific into the Indian Ocean. Estimates of the mean transport of the Indonesian Throughflow (IT) range from 2 to more than 20 Sv ( $\text{Sv} = 10^6 \text{ m}^3 \text{ s}^{-1}$ ), the large variability a consequence of the lack of direct observations and the IT's large seasonal-to-interannual variability (Wyrki, 1961; Gordon, 1986; Godfrey et al., 1993; Meyers

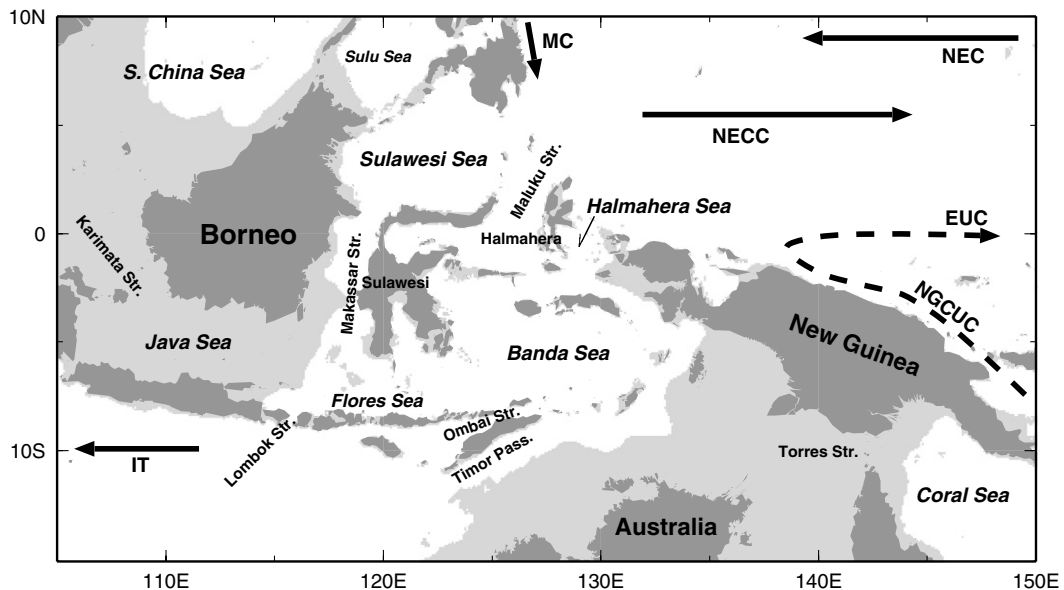


Fig. 1. Map of the Indonesian Seas, as well as nearby regions in the Pacific and Indian Oceans with areas shallower than 200 m lightly shaded. Solid arrows indicate major surface currents, including the Mindanao Current (MC), North Equatorial Current (NEC), and North Equatorial Countercurrent (NECC), as well as the Indonesian Throughflow (IT). The dashed arrow indicates the New Guinea Coastal Undercurrent (NGCUC) and Equatorial Undercurrent (EUC).

et al., 1995; Schiller et al., 1998; Potemra, 1999; Lebedev and Yaremchuk, 2000). More recent estimates, however, favor a value near the middle of this range (Gordon et al., 1999; Vranes et al., 2002; Susanto and Gordon, 2005). Most of the transport exits in the upper ocean above 400 m and comes from the North Pacific (Gordon and Fine, 1996; Gordon et al., 1999; Field et al., 2000; Gordon, 2005); there is also a deep relative maximum, consisting primarily of water from the South Pacific (Molcard et al., 1996; Talley and Sprintall, 2005; Gordon, 2005).

Since the North Pacific is essentially closed, source waters for the IT necessarily originate from the South Pacific, specifically from the intrusion of Antarctic Circumpolar (ACC) water into the basin (McCartney, 1977, 1982; Talley et al., 1996; Gordon and Fine, 1996). Much of it is entrained into the Subtropical Gyre (STG) in the far-eastern South Pacific as an upper part of Antarctic Intermediate Water (AAIW), and subsequently advects around the gyre as a tongue of low-salinity and high-oxygen water within the South Equatorial Current (SEC).

The SEC bifurcates at the Australian coast, with water in its northern part flowing equatorward and in its southern part returning to midlatitudes. The deep equatorward branch flows continuously along the Australian coast, eventually joining the deep part of the New Guinea Coastal Undercurrent (NGCUC) that extends to a depth of 900 m or more (Lindstrom et al., 1987, 1990; Tsuchiya, 1991; Qu and Lindstrom, 2002). Thereafter, AAIW spreads throughout the tropics (Reid, 1965, 1997; Talley, 1999; Zenk et al., 2005). There is evidence that AAIW also flows into the North Pacific (Rochford, 1960; Reid, 1965; Tsuchiya, 1991; Fine et al., 1994), as part of the northward-flowing Mindanao Undercurrent (Hu et al., 1991; Qu et al., 1998). Recent observations indicate that AAIW does not extend as a distinct water mass much farther north than 15°N in the western North Pacific (Qu et al., 1999; Qu and Lindstrom, 2004); farther north, it loses its distinguishing salinity minimum, and its fate remains unknown.

Another prominent, subthermocline water mass is thermostad water, located just beneath the near-equatorial thermocline. Like AAIW, it also originates in the South Pacific, either from water subducted north of New Zealand (Tsuchiya, 1991; Roemmich and Cornuelle, 1992) or from Subantarctic Mode Water (SAMW) generated in the eastern South Pacific (Toggweiler et al., 1991). In either case, the subducted water may still arise from the ACC, via near-surface northward flow that is modified by surface fluxes before it subducts; it could also originate within the Pacific via southward flow of near-surface water from the tropics, forming an overturning cell within the basin that is somewhat broader and deeper than the South Pacific Subtropical Cell (McCreary and Lu, 2001).

## 1.2. Models

Models have contributed significantly toward understanding impacts of the IT-associated, Interocean Circulations (IOCs) in both the Indian and Pacific Oceans (see Godfrey, 1996, for a review). The models vary in their domain size, including models confined to the Indian Ocean (McCreary and Kundu, 1987; Godfrey and Weaver, 1991; Hughes et al., 1992) and Pacific Ocean (Lu et al., 1998; McCreary and Lu, 2001; McCreary et al., 2002) in which the IT is externally prescribed, as well as global models in which it is generated internally (Miyama et al., 1995; Verschell et al., 1995; Shriver and Hurlburt, 1997; Murtugudde et al., 1998; Rodgers et al., 1999; Schneider, 1998; Lee et al., 2002).

Hirst and Godfrey (1993, 1994) compared solutions with open and closed Indonesian passages in their global, Ocean General Circulation Model (OGCM), the difference between the two solutions measuring the IT-associated flow. Among other results in their remarkably comprehensive study, the authors identified basic dynamical processes involved in IT-associated circulations, namely, the radiation of Kelvin and Rossby waves and their damping by diapycnal mixing processes (vertical diffusion, upwelling and subduction, and convective overturning; see Section 3).

McCreary and Lu (2001) examined the IT's influence on the circulation of Pacific subthermocline waters using a  $4\frac{1}{2}$ -layer model of the Pacific Ocean forced by winds and an externally prescribed IT with transport  $M$ . In their solutions, it was the IT that forced significant flow of South Pacific, subthermocline water into the tropics, both thermostad water (layer 3) and AAIW (layer 4): with  $M = 0$ , the tropics filled with water from the North Pacific in layer 3, the model's representation of North Pacific Intermediate Water (NPIW), and the transport of AAIW into the northern hemisphere reduced by an order of magnitude. McCreary

et al. (2002) improved the vertical-mixing parameterization of the McCreary and Lu (2001) model (see Appendix A), allowing the system to develop subsurface countercurrents (Tsuchiya, 1975; Tsuchiya Jets, TJs) within layer 3, which were forced by upwelling along the South American coast and in the Costa Rica dome. With  $M = 0$ , the layer 3 upwelling regions, as well as the TJs, vanished, suggesting that upwelling of subthermocline water in the eastern, equatorial Pacific is an important branch of the IT-associated circulation in the Pacific.

Since the South Pacific waters that supply the IT are deep, it is noteworthy that the IT is so surface trapped. A possible explanation for the trapping is the shallow sills of the Indonesian Seas. On the other hand, the observed IT is considerably more surface trapped (upper 400 m) than the deepest direct pathway through the Indonesian Seas ( $\sim 1500$  m), suggesting another cause. Wajsowicz (1995) obtained a suite of solutions to an OGCM with and without stratification and bottom topography that addresses this issue. In her two stratified solutions, the IT remained surface trapped even when all sills were removed from the Indonesian Seas; the major change from the solution with sills was that the IT transport increased from about 6 Sv to 7 Sv, with all the additional transport occurring at depth (compare her Figs. 10a and 14a). This result points towards baroclinic processes in the interior of the Pacific and Indian Oceans as being important factors in determining the IT depth; in particular, since the South Pacific inflow extends to intermediate depths, it suggests the importance of Pacific upwelling.

### 1.3. Present research

In this study, we continue the modeling effort to understand the interaction of the IT with Indo-Pacific circulations. As such, our discussion necessarily involves surface and subsurface flows in both basins, but our focus is on the IT's interaction with subthermocline (thermostad) and upper-intermediate (AAIW) circulations in the Pacific. We consider questions like the following: what processes determine the IT's vertical structure and source waters? Why does the South Pacific inflow extend to intermediate depths, whereas the IT outflow is primarily surface trapped in the upper 400 m with a secondary, deep core? What processes transform the cool, deep South Pacific inflow to warm, shallow IT water, and vice versa? What are the pathways of IT-associated, subsurface flows in the Pacific?

We obtain solutions to three different model types: a linear, continuously stratified (LCS) model and a non-linear,  $4\frac{1}{2}$ -layer model (LOM), both confined to the Indo-Pacific basin; and a global OGCM developed at the Center for Climate System Research, University of Tokyo (COCO). The models cover a range of dynamical complexity, with solutions to the LCS model providing the foundation needed to understand the basic dynamics of IT-associated flows, LOM including nonlinear processes and allowing for realistic representation of upwelling and subduction, and COCO including explicit thermohaline processes and bottom topography. The comparison of solutions to the three model types is therefore instructive, allowing the strengths and weaknesses of each model to be more readily assessed. Perhaps most importantly, the models differ in the nature of their diapycnal mixing processes. As we shall see, these processes are key factors for determining the vertical profile of the IT within the Indonesian Seas, the regions where water upwells and subducts throughout the basin, and the structure of solutions' subsurface flow fields.

Solutions are obtained with both open and closed Indonesian passages. Let  $Q$  be the label of a solution associated with a particular model or parameter set. Throughout the text, we refer to corresponding solutions with open and closed passages as Solutions  $Q$  and  $Q'$ , respectively, and to their difference (Solution  $Q$  – Solution  $Q'$ ) as Solution  $\Delta Q$ ; fields from the three solutions are labelled  $q$ ,  $q'$ , and  $\Delta q$ . Solutions  $\Delta Q$  are essentially “driven” by the flow across the Indonesian passages,  $v_a$  (defined precisely in Section 3.1), and hence are useful for isolating the flow fields generated by the IT in both basins. In contrast, Solutions  $Q$  and  $Q'$  are required for understanding the processes that determine the vertical structure of  $v_a$  and for identifying actual pathways of water parcels. For each model, Solution  $\Delta Q$  is described in detail, with prominent features of Solutions  $Q$  and  $Q'$  reported as needed.

The paper is organized as follows. In Section 2 and Appendix A, we describe the three models. Section 3 reports solutions to the LCS model, discussing the basic processes that determine their spin-up (Section 3.1), equilibrium state (Section 3.2), and the vertical structure and source waters of the IT (Section 3.3). Sections 4 and 5 then present the more realistic solutions to LOM and COCO, focusing on Pacific subsurface circulations. Section 6 provides a summary and discussion of results.

Our study is most closely related to those of Hirst and Godfrey (1993, 1994) and McCreary and Lu (2001). Indeed, our discussion of basic IT dynamics using the LCS model (Sections 3.1 and 3.2) was inspired by the simplified (modal) solutions reported in Hirst and Godfrey (1994). Our LOM solutions (Section 4) are an extension of the Pacific-basin solutions of McCreary and Lu (2001) and McCreary et al. (2002) to an Indo-Pacific domain in which the IT is internally generated rather than externally prescribed. Finally, our discussions of difference solutions, particularly for the LCS model, can be viewed as a contribution to the literature on the global response to a prescribed mass source in one ocean basin (e.g. Huang et al., 2000; Johnson and Marshall, 2004; Cessi et al., 2004), except that the IT provides both a source for the Indian Ocean and a compensating sink for the Pacific.

## 2. The ocean models

### 2.1. LCS model

The LCS model is an extension of the Indian Ocean model of McCreary et al. (1996) to an Indo-Pacific domain. It is a linearization of the primitive equations about a background state of rest with Brunt–Vaisala frequency,  $N_b(z)$ . The ocean bottom is assumed flat at a depth of  $D = 4500$  m, and Laplacian, horizontal mixing is included with a coefficient  $\nu_h = 3 \times 10^7$  cm<sup>2</sup>/s. For three of the solutions reported here (Solutions A–C), the vertical mixing is second order in  $z$  with a coefficient of the form  $\nu = A/N_b^2(z)$ , but two solutions utilize fourth-order mixing (Solutions D and E; defined in Section 3.3.1). With this restriction on  $\nu$ , solutions can be represented as expansions in the vertical normal modes of the system,  $\psi_n(z)$ , each mode associated with a characteristic speed,  $c_n$ , and normalized so that  $\psi_n(0) = 1$ . The response of each mode is obtained numerically on a C-grid with a horizontal resolution of  $0.5^\circ$ , and the complete solution is a sum of the contributions from all of the modes. In principle, there are an infinite number of modes in the expansions. For the solutions shown here, the expansions are truncated at a finite value  $n = 30$ , a value large enough for solutions to be well converged. (See McCreary, 1985, for a general review of models of this sort).

Our standard buoyancy frequency is given by,

$$N_b(z) = B e^{bz} + C, \quad (1)$$

where  $b^{-1} = 1000$  m,  $B = 55 \times 10^{-4}$  s<sup>-2</sup> and  $C = 6.32 \times 10^{-4}$  s<sup>-2</sup>, an idealized version of the average buoyancy frequency throughout the Indo-Pacific basin based on data from the World Ocean Atlas 94 (WOA94; Levitus, 1994). Solutions are also obtained when  $N_b$  is the average buoyancy frequency near the equator (from  $5^\circ\text{S}$  to  $5^\circ\text{N}$  and  $40^\circ\text{E}$  to  $60^\circ\text{W}$ ) determined from the WOA94 data (see Section 3.3.1 and Fig. 6 below). Unless specified otherwise  $A = 3.8 \times 10^{-5}$  cm<sup>2</sup>/s<sup>3</sup>; with this choice,  $\nu$  varies from 1.0 cm<sup>2</sup>/s at the ocean surface (where  $N_b^2$  is a maximum) to 5.4 cm<sup>2</sup>/s at a depth of 1000 m. Table 1 lists values of  $c_n$ , and other quantities defined below, for the first 10 modes.

Table 1  
Parameter values for modes 1–10 of LCS model

Parameter	$n$									
	0	1	2	3	4	5	6	7	8	9
$c_n$ (cm/s)	21,000	261	130	87	66	53	44	38	33	29
$\mathcal{H}_n$ (m)	4500	632	673	680	679	678	677	677	677	677
$Z_n$	1.00	0.93	0.74	0.49	0.23	0.02	-0.12	-0.16	-0.14	-0.08
$T_n$ (years)	0.001	6.5	26	58	101	157	227	304	404	523
$t_n$ (years)		57	14	6.4	3.7	2.4	1.6	1.2	0.92	0.71
$c_n^3/A$ (1000 km)		4700	580	160	76	40	23	15	9.6	6.5
$L_{rn}$ (1000 km)		53	3.3	0.66	0.22	0.09	0.04	0.02	0.01	0.008

Values of  $c_n$  correspond to the  $N_b(z)$  profile defined in (1). Coefficients  $Z_n$  are determined from profile (2) with  $z_1 = -200$  m and  $z_2 = -400$  m, so that  $Z(z)$  approximates the vertical structure of the upper core of the IT. The dynamical time scale  $T_n$ , defined in (3), is the time it takes a mode- $n$  Rossby-wave to cross the width of the basin ( $L = 6000$  km) at latitude  $30^\circ\text{S}$ . The quantity  $t_n = c_n^2/A$  is the damping time scale for mode  $n$ , and  $c_n^3/A$  and  $L_{rn} = c_n t_n = (\beta/f^2)(c_n^4/A)$  are the damping length scales for Kelvin waves and for Rossby waves at  $|\gamma| = 30^\circ$ , respectively, each with  $A = 3.8 \times 10^{-5}$  cm<sup>2</sup>/s<sup>3</sup>.

Solutions are obtained in a basin covering the Indo-Pacific domain from 60°S to 60°N and 20°E to 60°W, and South America and Africa are artificially joined at the 20°E/60°W boundary. Land points are located wherever the ocean depth is shallower than 200 m in the TerrainBase data (Row et al., 1995). Exceptions are that the Lombok and Ombai Straits are closed so that all the IT passes through the Timor Strait (Fig. 1), the passages from the South China Sea to the Indonesian Seas are closed, and “small” islands are everywhere neglected. No-slip conditions are applied at all coastal boundaries, and cyclic boundary conditions are imposed along the 20°E/60°W boundary south of the southern tip of Africa.

Most solutions are forced by the annual-mean wind stress,  $\bar{\tau}$ , determined from the Hellerman and Rosenstein (HR; 1983) climatology. Additional test runs are forced either by the ECMWF climatology averaged from December 1978 to February 1994 (ERA15; Gibson et al., 1999) or the 6-year, QuikSCAT climatology averaged from January 2000 through December 2005.

Wind stress is introduced into the model as a body force,  $\bar{\tau}Z(z)$ , where

$$Z(z) = \frac{2}{|z_1 + z_2|} \begin{cases} 1 & z > z_1, \\ \frac{z - z_2}{z_1 - z_2} & z_1 \geq z > z_2, \\ 0 & z_2 \geq z, \end{cases} \quad (2)$$

$z_1 = -50$  m, and  $z_2 = -100$  m. According to (2),  $Z(z)$  is constant to a depth of 50 m and decreases linearly to zero at a depth of 100 m. The contribution of  $\bar{\tau}$  to each mode is then  $\phi_n \bar{\tau}$ , where  $\phi_n = Z_n / \mathcal{H}_n$ ,  $Z_n = \int_{-D}^0 Z(z) \psi_n(z) dz$ , and  $\mathcal{H}_n = \int_{-D}^0 \psi_n^2(z) dz$ .

Wind-forced solutions are obtained both with the Indonesian passages open and closed at 8.75°S. Solutions for the baroclinic modes and barotropic mode are integrated for 100 and 5 years, respectively, by which time they are essentially in equilibrium. The solutions reported in Section 3 are annual averages taken from the final year of their integration.

## 2.2. LOM

The 4½-layer model (LOM) is an extension of the McCreary and Lu (2001), Pacific Ocean model to a larger basin that includes the Indian Ocean and the ACC. The horizontal resolution of the grid is 0.5°, and basin boundaries are specified as for the LCS model. Although LOM allows for density to vary within each layer, in this version densities are fixed to constant values of 23, 25, 26.8 and 27.2  $\sigma_\theta$  in the four active layers and the density of the deep ocean is 27.8  $\sigma_\theta$ . With these choices, each layer corresponds to a particular water-mass type, namely, near-surface tropical water, thermocline water, subthermocline water, and upper-intermediate water, the latter two corresponding to NPIW in the northern hemisphere and to AAIW in the southern hemisphere, respectively.

There is horizontal viscosity with the coefficient  $\nu_h = 3 \times 10^7$  cm<sup>2</sup>/s. Across-layer velocities provide all the diapycnal mixing in the model. Almost all of the exchange occurs in regions where layer thicknesses tend to become thinner or thicker than specified values, thereby allowing for the processes of upwelling and subduction; there are also weak terms in each layer corresponding to the linear damping of the LCS system, and special treatment is required to allow for the ACC region (see Appendix A). Note that because layer temperatures (densities) are not allowed to vary, LOM cannot represent thermodynamic processes (subduction and convection), a model limitation that is overcome in COCO. To represent the effect of extratropical cooling, subduction is limited to occur poleward of prescribed latitudes, and extends to deeper layers farther poleward [see the discussion of Eq. (A1b)].

Solutions are forced by the monthly climatological, ERA15 wind stress, and are obtained with the Timor Strait open (Solution LOM) and closed at 8.75°S (Solution LOM'). Solution LOM' is spun up from an initial state of rest for 210 years. Initial layer thicknesses for layers 1–4 are 40, 40, 350 and 650 m, respectively, for a total thickness of  $H = 1080$  m. During the integration, the masses of individual layers can vary due to across-layer exchange, but collectively they maintain an average thickness of  $H$ , that is, the total mass of the model ocean is conserved. Solution LOM is started from the year-100 state of Solution LOM' and integrated until year 210. The solutions presented in Section 4 are 10-year averages from years 200–210, the long averaging time needed to bring out mean currents in regions of intense eddy activity.

### 2.3. COCO

The level model is the version of COCO used by Nakano (2000) and Nakano and Sugimoto (2002a,b). It solves a finite-difference form of the standard hydrostatic, Boussinesq, primitive equations in a global domain without the Arctic Ocean and with realistic bottom topography. Its horizontal resolution is  $1^\circ \times 1^\circ$ , and there are 40 levels in the vertical with a resolution of 50 m near the surface, gradually decreasing to 200 m near the bottom. A third-order, one-dimensional scheme based on quadratic upstream interpolation (QUICKEST; Leonard, 1979) is used for the vertical advection of temperature and salinity, and its two-dimensional extension (UTOPIA; Leonard et al., 1993, 1994) is used for horizontal advection. Bottom topography is determined almost everywhere by a simple interpolation of the ETOPO5 data set (National Geophysical Data Center, 1988) onto the model grid. The exception is in the Indonesian Seas, where the interpolation badly misrepresents shallow sills and, hence, resulted in unrealistic circulations. In the Indonesian Seas, then, bottom topography is modified to be similar to that used for the LCS model and LOM, except with an open passage from the South China Sea to the Flores Sea through the Java Sea.

Horizontal viscosity is uniformly  $2.5 \times 10^8 \text{ cm}^2/\text{s}$ . Vertical viscosity is  $10 \text{ cm}^2/\text{s}$  at the sea surface, decreases to  $1.0 \text{ cm}^2/\text{s}$  at 150 m, and remains constant thereafter. The model includes three forms of horizontal diffusion: isopycnal diffusion, Gent and McWilliams (1990) thickness diffusion, and background horizontal diffusion with coefficients of  $10^7$ ,  $7 \times 10^6$ , and  $1 \times 10^6 \text{ cm}^2/\text{s}$ , respectively. Outside the tropical Pacific, vertical diffusivity is  $0.1 \text{ cm}^2/\text{s}$  from the surface to 500 m and gradually increases to  $2.7 \text{ cm}^2/\text{s}$  near the bottom. Simulations of TJs in coarse-resolution OGCMs require low levels of vertical diffusion (Furue et al., 2007). We therefore reduce vertical diffusivity in the tropical Pacific by a factor  $\gamma$  that is 0 for  $|y| < 20^\circ$  and  $|z| < 400 \text{ m}$ , 1 for  $|y| \geq 30^\circ$  or  $|z| \geq 800 \text{ m}$ , and ramps smoothly between the two regions.

The model is forced by monthly climatological HR wind stress, a Haney (1971) condition for SST based on da Silva et al. (1994) data, and the fresh-water flux of da Silva et al. (1994). In addition, sea-surface salinity is weakly restored to Levitus (1994) climatological values with a time scale of 200 days.

Starting from the final state of Nakano and Sugimoto (2002b) solution, we integrate the model for 550 years using their bottom topography and the above mixing specifications with  $\gamma = 1$ , using momentum acceleration (Bryan, 1984) over the entire ocean depth and tracer acceleration below 1000 m during the first 500 years followed by synchronous (unaccelerated) integration during the last 50 years. The synchronous integration is then continued with variable  $\gamma$  for 50 years. From the final state of this spin-up run, we integrate the model for another 80 years with the modified topography (Solution COCO). Also from the same final state of the spin-up run, we obtain another 80-year solution in which the Indonesian passages are closed at  $8.5^\circ\text{S}$  (Solution COCO'). Annual averages from the final years of the two solutions are reported in Section 5.

## 3. Solutions to the LCS model

In this section, we first discuss basic dynamics of IT-associated flows in the LCS model, describing the spin-up of solutions when the Indonesian passages are abruptly opened (Section 3.1) and their steady-state response (Section 3.2). We conclude with a discussion of the processes that determine the spatial structure of the currents within the Indonesian Seas (Section 3.3), finding that the IT vertical structure and source waters are remotely determined by properties of the Pacific circulation.

### 3.1. Spin-up

Consider the response when the ocean is initially in an equilibrium state forced by  $\bar{\tau}$  with closed Indonesian passages and the passages are abruptly opened. In the Pacific Ocean, some Rossby waves north of New Guinea (or Halmahera), which otherwise reflect back into the Pacific, now propagate into the Indian Ocean; similarly, in the Indian Ocean some Kelvin waves that reflect from the eastern boundary now enter the Indonesian Seas and eventually the Pacific Ocean. Let  $v_a(x, y_a, z)$  be the resulting steady-state meridional current through the Indonesian passages (Timor Strait) at  $y_a = 8.75^\circ\text{S}$  from a solution with open passages. Since the waves that

establish  $v_a$  are baroclinic, as well as barotropic, we can expect that  $v_a$  will have a vertical structure that varies prominently with depth.

Let  $v_{an}(x, y_a)$  be the contribution to  $v_a$  from mode  $n$ , and consider the response of a particular vertical mode when  $v_{an}$  is switched on and there is no wind forcing. Because the LCS model is linear, this response is the *negative* of the flow that adjusts the steady state of the open-passage solution to that of the closed-passage solution. (It is not the same as the reverse adjustment when the passages are opened, since the flow through the Timor Strait is equal to  $v_{an}$  only in steady-state; however, the two adjustments are very similar, as the throughflow adjusts to be close to  $v_{an}$  shortly after the passages are opened.) Each mode of the system responds to  $v_{an}$  by radiating waves away from the Indonesian passages. Because barotropic waves propagate so rapidly, the barotropic response adjusts to equilibrium in only a few days' time. Here, we describe the slower baroclinic response, first considering the inviscid response of a particular baroclinic mode and then noting the effects of diffusion.

In response to the Indian Ocean mass source, coastal Kelvin waves initially propagate eastward along the coast of Indonesia, causing pressure  $\Delta p_n$  to increase across the passages by  $\delta p_n = \bar{\rho} f_a V_{an}$ , where  $f_x = f(y_x)$ ,  $V_{an} = \int_{\mathcal{C}} v_{an} dx$ , and  $\mathcal{C}$  is a contour along latitude  $y_a$  that includes only the Indonesian passages. In the next few weeks, the Kelvin waves radiate down the west coast of Australia, and Rossby waves begin to propagate westward from the coast. After their passage, pressure is adjusted to  $\delta p_n$  everywhere along the western and southern coasts of Australia and behind the Rossby-wave front. It follows from geostrophy that the integral of the surface velocity across the current around Australia is  $V_{bn} = |\delta p_n / (\bar{\rho} f_b)| = |(f_a / f_b) V_{an}|$ , where  $y_b$  is the latitude of the southern tip of Australia. Note that  $V_{bn} < |V_{an}|$  since  $f_a / f_b < 1$ , the rest of the flow being carried west by the Rossby waves.

Subsequently, the Rossby waves propagate across the Indian Ocean at all latitudes north of  $y_b$ . They reflect equatorward along the African coast, eastward along the equator, and poleward along the eastern boundary via coastal and equatorial Kelvin waves, and then westward as another Rossby-wave packet. These processes continue to increase  $\Delta p_n$  throughout the Indian Ocean until  $\Delta p_n + \delta p_n$  at the tip of Australia is large enough to allow  $V_{bn} = |V_{an}|$  (Johnson and Marshall, 2004). A measure of the minimum time needed for this adjustment is the time it takes a baroclinic Rossby-wave to cross the basin at latitude  $y_b$ , that is,

$$T_n = L / c_m(y_b), \quad (3)$$

where  $c_m(y_b) = \beta c_n^2 / f_b^2$  and  $L$  is the width of the basin at  $y_b$ . We emphasize that  $T_n$  represents only a *minimum* adjustment time, since multiple reflections of Rossby and equatorial Kelvin waves are required before the system reaches equilibrium. Table 1 lists values of  $T_n$  for the first 10 modes for  $y_b = 30^\circ\text{S}$  and  $L = 6000$  km.

Similar adjustments take place in the Pacific Ocean, in this case tending to decrease  $\Delta p_n$ . They would also eventually lead to a transport around Africa equal to  $V_{an}$ , except that sometime after  $T_n$  the mass sink in the Pacific ( $-|V_{an}|$ ) is balanced by the flow around Australia ( $|V_{an}|$ ), and waves in the Pacific are then no longer directly forced by a loss of mass. Thereafter, a final stage of adjustment occurs as these free waves radiate about the Pacific basin and into the Indian Ocean, eventually decreasing  $\Delta p_n$  uniformly throughout both basins, and eliminating the flow around Africa. The resulting, inviscid, steady-state balance for each baroclinic mode has the same structure as that of the barotropic mode (top panel of Fig. 2 below).

When diffusion is included, similar dynamical adjustments occur except that the baroclinic waves are damped. The damping time scale for each mode is  $t_n = c_n^2 / A$ , resulting in spatial decay scales of  $c_n^3 / A$  for Kelvin waves and  $L_m(y) = c_m(y) t_n = (\beta / f^2) (c_n^4 / A)$  for Rossby waves (Table 1). Because of their high propagation speed, the Kelvin-wave decay scales are greater than basin scale for several low-order modes ( $n \leq 4$ ); however, the decay scales for the slower-propagating Rossby waves at midlatitudes (at  $30^\circ\text{S}$ , say) are greater than basin scale only for the  $n = 1$  mode.

Based on the above, we define a measure of the spin-up time for each mode to be the *smaller* of  $T_n$  and  $t_n$ . A measure of the spin-up time for the complete system,  $T$ , is the *largest* of the spin-up times for each mode. For our standard parameter choices, the system spin-up time is  $T = t_2 = 14$  years (Table 1). Time  $T$  is sensitive to mixing strength: when  $A \rightarrow A/4$ , for example,  $t_n$  values increase by a factor of 4 and hence  $T = T_2 = 26$  years; when  $A \rightarrow A/10$ ,  $T = T_3 = 58$  years.

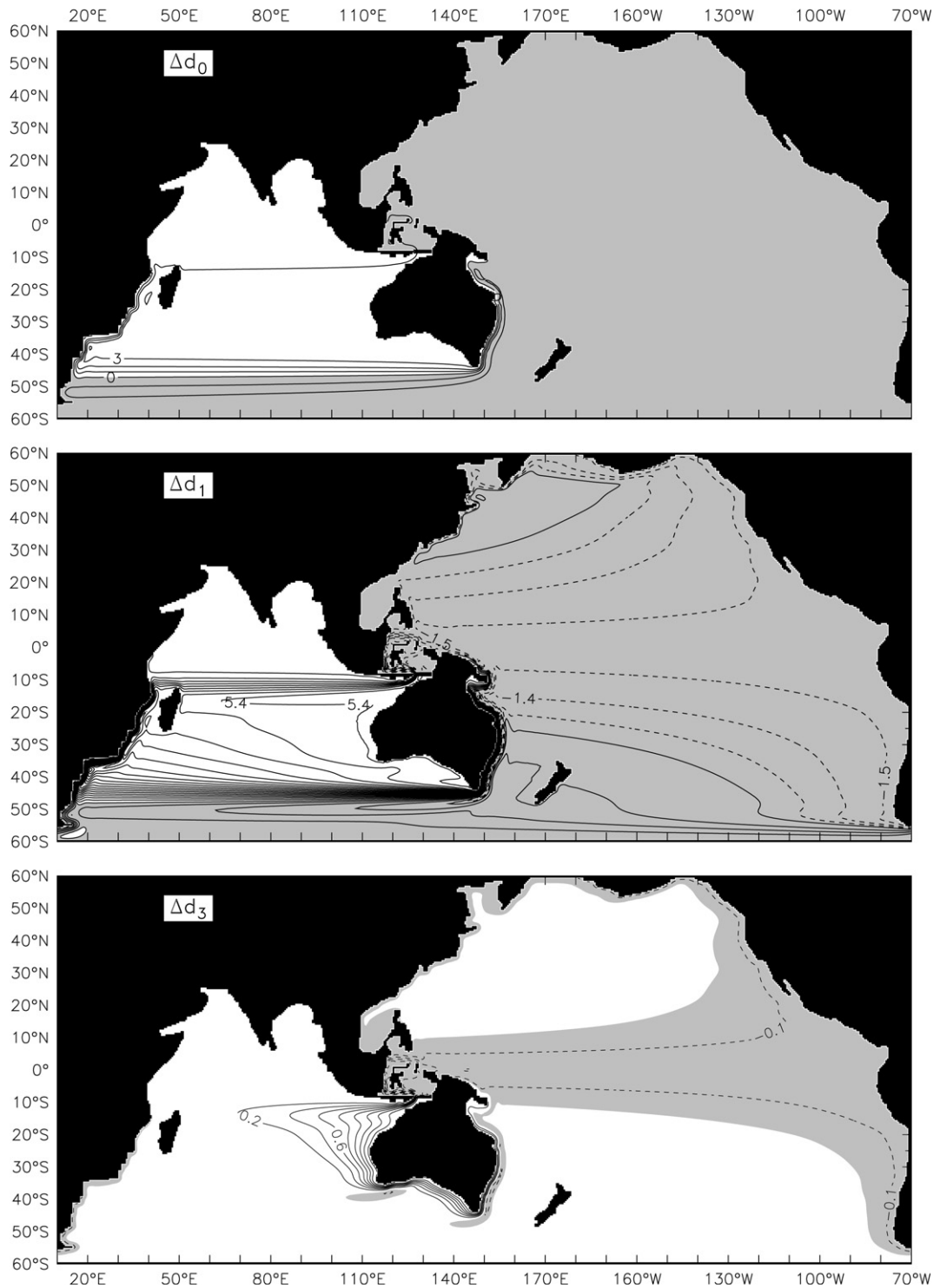


Fig. 2. Horizontal maps of sea level  $\Delta d_n$  associated with the  $n = 0$  (top), 1 (middle), and 3 (bottom) modes from Solution  $\Delta A$ . Contour intervals are 1 cm in the top panel, 0.3 cm (solid) and 0.1 cm (dashed) in the middle panel, and 0.2 cm (solid) and 0.1 cm (dashed) in the bottom panel. Cyclic boundary conditions are applied along 60°W/20°E, and the region from 70°W to 60°W is plotted at the left hand side of the figure.

3.2. Steady-state response

Fig. 2 plots the steady-state, surface pressure fields for the first three modes when  $v_a(x, y_a)$  is obtained from the solution with open passages that uses the standard values of  $v$  and  $N_b$  (Solution A). The plots thus show the response of the difference between solutions with open and closed passages (Solution  $\Delta A$ ). The fields are plotted in terms of sea level, that is,  $\Delta d_n = \Delta p_n/g$ .

Barotropic sea level,  $\Delta d_0$ , is uniformly high in the Indian Ocean south of  $y_a$  and north of  $y_b$ , and low throughout the Pacific Ocean. (Hirst and Godfrey, 1993, derived an analytic solution that can be applied to any inviscid mode. It supports the structure of  $\Delta d_0$ .) The patterns change markedly with  $n$ , becoming increasingly coastally trapped to the west coasts of Australia and the Americas, a consequence of the damping of baroclinic Rossby waves (e.g. Hirst and Godfrey, 1993, 1994; Huang et al., 2000). Note that  $\Delta d_n$  is essentially constant along the west coasts, since the Kelvin-wave decay scale,  $c_n^3/A$ , is so large for these low-order modes (Table 1). Higher-order modes exhibit greater trapping, with even Kelvin waves decaying significantly away from the source and sink regions. The patterns also decrease in amplitude, since their amplitude is proportional to  $\phi_n = Z_n/\mathcal{H}_n$  (Table 1).

As expected, the structure of  $\Delta d_0$  shows that there is an anticyclonic, barotropic circulation around the southern Indian Ocean with a northward branch along the east Australian coast. In contrast, the damping of baroclinic Rossby waves away from the eastern boundary allows baroclinic geostrophic currents to exist in the interiors of both oceans wherever there is a gradient of  $\Delta d_n$ . Consider the flow field associated with the  $n = 1$  mode (middle panel of Fig. 2). In the Indian Ocean, water in the upper ocean (i.e., above the zero crossing of  $\psi_1$ ) diverges from the westward jet along 10–15°S and from the southward western boundary current along Africa, flowing southeastward across the basin either to the Australian coast or the ACC. In contrast, upper ocean water in the Pacific Ocean flows westward and equatorward across the basin in both hemispheres, supplied either by upwelling or by flow around South America/Africa. There are opposite-directed currents in the deep ocean (below the zero crossing of  $\psi_1$ ). A related consequence of diffusion is the existence of downwelling throughout the Indian basin and upwelling throughout the Pacific: these vertical velocities have the vertical structure  $\int_{-D}^z \psi_1(z') dz'$  and their strength is proportional to  $\Delta d_1$ . Similar flows exist for the other baroclinic modes (e.g., bottom panel of Fig. 2), albeit with more complex vertical structures and with increased trapping to the source and sink regions.

Fig. 3 plots the total sea-level response from all the modes,  $\Delta d$ . The dominant contribution from the  $n = 1$  mode is apparent, with the higher-order modes increasing  $|\Delta d|$ , and hence the surface geostrophic currents, offshore from Australia and in the tropical Pacific. Contributions from the higher-order modes tend to trap

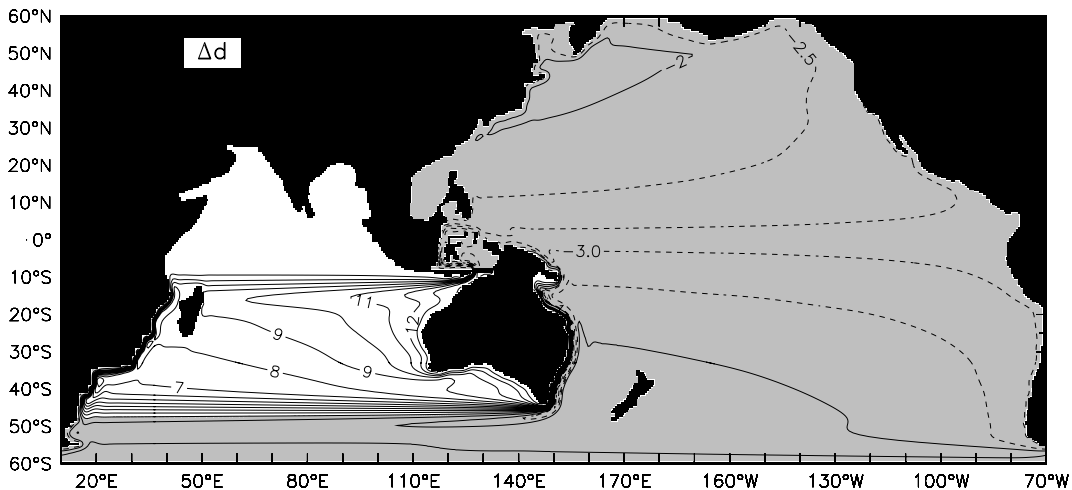


Fig. 3. Horizontal map of the total sea level  $\Delta d$  from Solution  $\Delta A$ . Contour intervals are 1 cm (solid) and 0.5 cm (dashed). Cyclic boundary conditions are applied along 60°W/20°E, and the region from 70°W to 60°W is plotted at the left hand side of the figure.

the flow field nearer to the surface, rather than to introduce additional current reversals. As for the mode-1 response, then, subsurface flows of the total response tend to be oppositely directed to the surface ones (except in the region where there are strong barotropic currents), becoming more surface trapped near Australia and in the tropical Pacific. Fig. 4 illustrates the trapping in the tropical, western Pacific, plotting  $\Delta u$  in a section from 20°S to 20°N along 160°E. Near the equator, the higher-order modes superpose to produce a near-surface westward jet overlying an eastward current centered about a depth of 400 m, with weak reversals at greater depths. It is worth emphasizing that this current structure is driven by  $v_a(x, y_a, z)$ , the flow across the Indonesian passages, not directly by the Pacific winds (see Fig. 7 below for a wind-driven response).

The interior currents in both oceans significantly impact the vertical structure of the currents that carry IT-associated transport. To illustrate this property, Fig. 5 plots transport/depth profiles through the Timor passage as well as at several locations across the Indian Ocean and along the western boundaries of Africa, Australia, and New Guinea. For each profile, the total (depth-integrated) transport is 18 Sv, since the currents include the barotropic flow. Consistent with the observations, the Timor profile is highly surface trapped with a subsurface core (see Section 3.3.1). In the Indian Ocean, the profiles show a weakening and deepening of the current away from Indonesia, a result of convergences and divergences by the interior baroclinic flow field, which drain

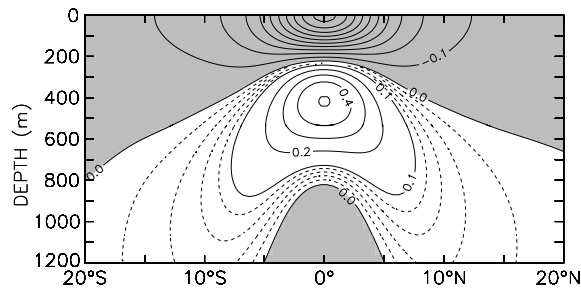


Fig. 4. Meridional section of zonal velocity from 20°S to 20°N along 160°E from Solution  $\Delta A$ . Contour intervals are 0.1 cm/s (solid) and 0.02 cm/s (dashed).

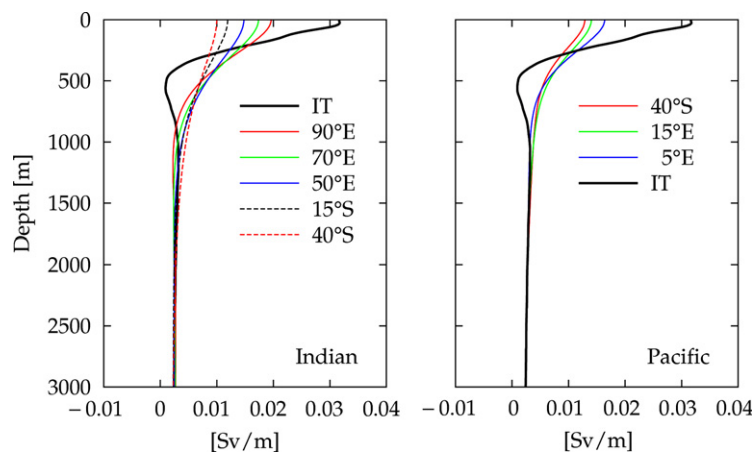


Fig. 5. Transport/depth profiles (Sv/m) for the currents that carry IT-associated transport in the Indian (left) and Pacific (right) Oceans from Solution  $\Delta A$ . The profiles are located across the Indonesian passages at 8.75°S (IT), across the Indian Ocean near 10°S (90°E, 70°E, and 50°E), along Africa (15°S and 40°S), and along the east coasts of Australia and New Guinea (40°S, 15°S, and 5°S). The profiles are all plotted as positive in the direction of the IT transport. The western boundary transports are obtained by integrating the alongshore current offshore from the coast to its second zero crossing (*i.e.*, including the offshore reverse flow of the Munk layer). The zonal currents across the Indian Ocean integrate the eastward flow from 15°S to 5°S.

upper ocean water from the western boundary current and supply water to it at depth. In the Pacific Ocean, the western boundary currents have the opposite tendency, becoming more surface trapped to the north due to shallow convergence and deep divergence. Note that much of the trapping occurs near the equator, where higher-order modes are less damped and, hence, the subsurface interior flows are stronger and more concentrated in the upper ocean (Fig. 4).

### 3.3. Indonesian Seas

#### 3.3.1. IT vertical structure

Fig. 6 illustrates the sensitivity of the IT vertical structure to the model's mixing and stratification parameters, plotting steady-state, IT transport/depth profiles across the Timor Strait, defined by  $V_a(z) = \int_{\mathcal{C}} v_a(x, y_a, z) dx$ , from four solutions forced by HR winds: a solution using the standard values of  $v$  and  $N_b$  (Solution A; black curve) and three solutions using the equatorial  $N_b$  but with different mixing, namely, standard mixing (Solution B; red curve), weak mixing with parameter  $A$  reduced by a factor of 10 (Solution C; green curve), and a form of fourth-order mixing in which  $A$  is replaced by  $A_n = A(c_5/c_n)^2$  and  $A$  has its standard value (Solution D; blue curve). A fifth solution is like Solution D, except forced by annual-mean ERA15 winds (Solution E; cyan curve). Although the profiles vary considerably with  $N_b$  and  $v$ , their depth-integrated transport (provided by the  $n = 0$  mode) is either 17 Sv or 15 Sv, in agreement with Island Rule (Godfrey, 1989) estimates for HR and ERA15 winds, respectively.

Solution A has strong flow in the upper 500 m, but also extends to the ocean bottom, with 11.6 Sv below 1000 m. The surface flow field is stronger and more surface trapped in Solution B, owing to the background thermocline being closer to the surface, but the deep transport below 1000 m is still substantial (10.7 Sv). In Solution C, the transport below 1000 m decreases considerably (5.7 Sv), a consequence of low-order, baroclinic modes being less damped and, hence, able to cancel the deep barotropic flow more effectively. An unpleasant side effect of this solution, however, is that its EUC is unrealistically thin (not shown) because high-order modes are insufficiently damped (McCreary, 1981). This problem is avoided in Solutions D and E, for which the damping of low-order (high-order) modes is weaker (stronger) while that for the middle-order modes ( $n \approx 5$ ), which contribute most to the EUC, remain relatively unchanged. Note that their profiles tend to near-zero values at the ocean bottom, so that almost all the IT transport occurs above 2000 m.

It is noteworthy that the IT has a surface-trapped core, and that model parameters can be adjusted so that most flow is confined to the upper ocean (Solutions D and E). These properties point toward the importance of remote baroclinic processes in setting the IT vertical structure, as implied by the Wajsowicz (1993) flat-bottom solutions (Section 1). Nevertheless, there is considerable deep transport in solutions with reasonable mixing strengths (Solutions A and B). For these solutions, interior baroclinic processes are *not* strong enough to trap the IT transport entirely to the upper ocean; hence, the shallow Indonesian sills would certainly be an important blocking factor for their deep IT.

A striking feature of all the profiles is a minimum of the IT transport somewhat below the ocean surface, which splits the IT into near-surface and subsurface cores, consistent with the observations (Molcard et al., 1996; Talley and Sprintall, 2005; Gordon, 2005). The minimum results from the draining of subsurface waters from the western-ocean boundary by eastward currents in the near-equatorial Pacific, so that they are not available to supply the IT. Fig. 7 illustrates these currents, plotting  $u(y, z)$  from Solution D in the tropics along 160°E, which is representative of the flow field all the way to the western boundary: the subsurface, eastward currents that most strongly impact the IT are the EUC and the TJ-like lobes that extend into the deeper ocean on either side of the equator. Note that the depth of the IT minimum is about 250 m (blue curve in Fig. 6), whereas the depth of the Equatorial Undercurrent (EUC) core is only 100 m, an indication that the influence of the TJ-like currents is significant. Finally, in solutions like Solutions A–C but forced by ERA15 winds (not shown), the weakening is so strong that there is a subsurface reversal of the IT. As we shall see, a subsurface reversal also occurs in Solution LOM and in a solution to an OGCM, but for deeper, subthermocline water (see Section 4). In support of these ideas, Miyama et al. (1995) reported that in their OGCM solution the flow in the Indonesian Seas was strongly influenced by the EUC; in addition, the IT transport had a distinct minimum at a depth of about 400 m, deeper than the core of the EUC at 180°E (see their Fig. 7 and Table 2).

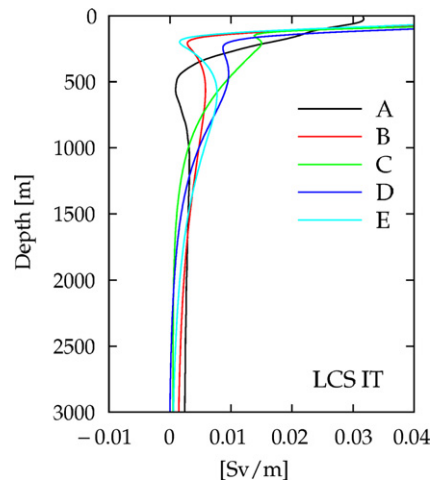


Fig. 6. Transport/depth profiles (Sv/m) of the IT from Solutions A–E defined in the text. The surface values of the curves for Solutions B–E are 0.060, 0.083, 0.075, and 0.055 Sv/m, respectively.

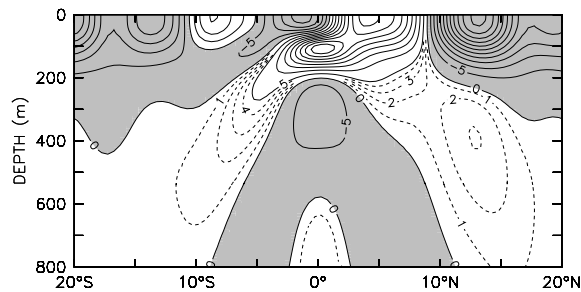


Fig. 7. Meridional section of zonal velocity from 20°S to 20°N along 160°E from Solution D. Contour intervals are 5 cm/s (solid) and 1 cm/s (dashed).

Table 2

Transports of IT-associated currents in Solution  $\Delta$ LOM

IT	Indian Ocean					Pacific Ocean			
	90°E	70°E	50°E	15°S	30°S	40°S	15°S	5°S	
Layer 1	−6.8	−5.5	−4.4	−2.1	−1.8	−0.1	2.9	2.2	2.8
Layer 2	−3.4	−4.7	−3.0	−6.2	−3.3	−2.8	1.9	3.4	2.8
Layer 3	0.4	−0.6	−2.5	−1.2	−3.7	−6.4	3.3	3.4	3.4
Layer 4	−2.7	−2.8	−3.7	−3.2	−3.1	−0.8	5.2	3.8	3.5
Total	−12.5	−13.5	−13.5	−12.6	−11.9	−10.1	13.3	12.8	12.5

Transport IT is obtained by integrating  $\Delta(h\nu_i)$  across the Indonesian passages at 8.75°S. The transports at 90°E, 70°E, and 50°E were obtained by integrating  $\Delta(h\nu_i)$  from 15.75°S to 7.25°S, 14.75°S to 5.75°S, and 12.25°S to 6.78°S, respectively. The remaining transports are for western boundary currents along the east coasts of Africa at 15°S and 30°S, Australia at 40°S and 15°S, and New Guinea at 5°S; they are obtained by integrating  $\Delta(h\nu_i)$  from the coast to 50°E, 38°E, 154°E, 156°E, and 153°E, respectively.

In all the solutions, the transport of the deep core (defined by the integration from the ocean bottom to the depth of the minimum transport) is too strong in comparison to the observations. In Solution D, for example, the deep-core transport is 11.8 Sv, larger than that of the shallow core (6.3 Sv). A possible reason for this discrepancy is the lack of bottom topography in the LCS model. Another possibility is the simplicity of the model's diapycnal mixing, which does not allow for significant draining of deeper waters from the western ocean; as we shall see, this deep draining is stronger in both the LOM and COCO solutions.

3.3.2. IT source waters

Fig. 8 illustrates the horizontal and vertical structures of the flow field in the Indonesian Seas for Solution D, plotting the streamfunction  $\psi$  of its barotropic mode (top panel), as well as velocity vectors at the surface (middle panel) and at 450 m (bottom panel) within the shallow and deep cores. There are two IT branches, a stronger one through the Makassar Strait and a weaker one that flows south of Halmahera to Sulawesi and

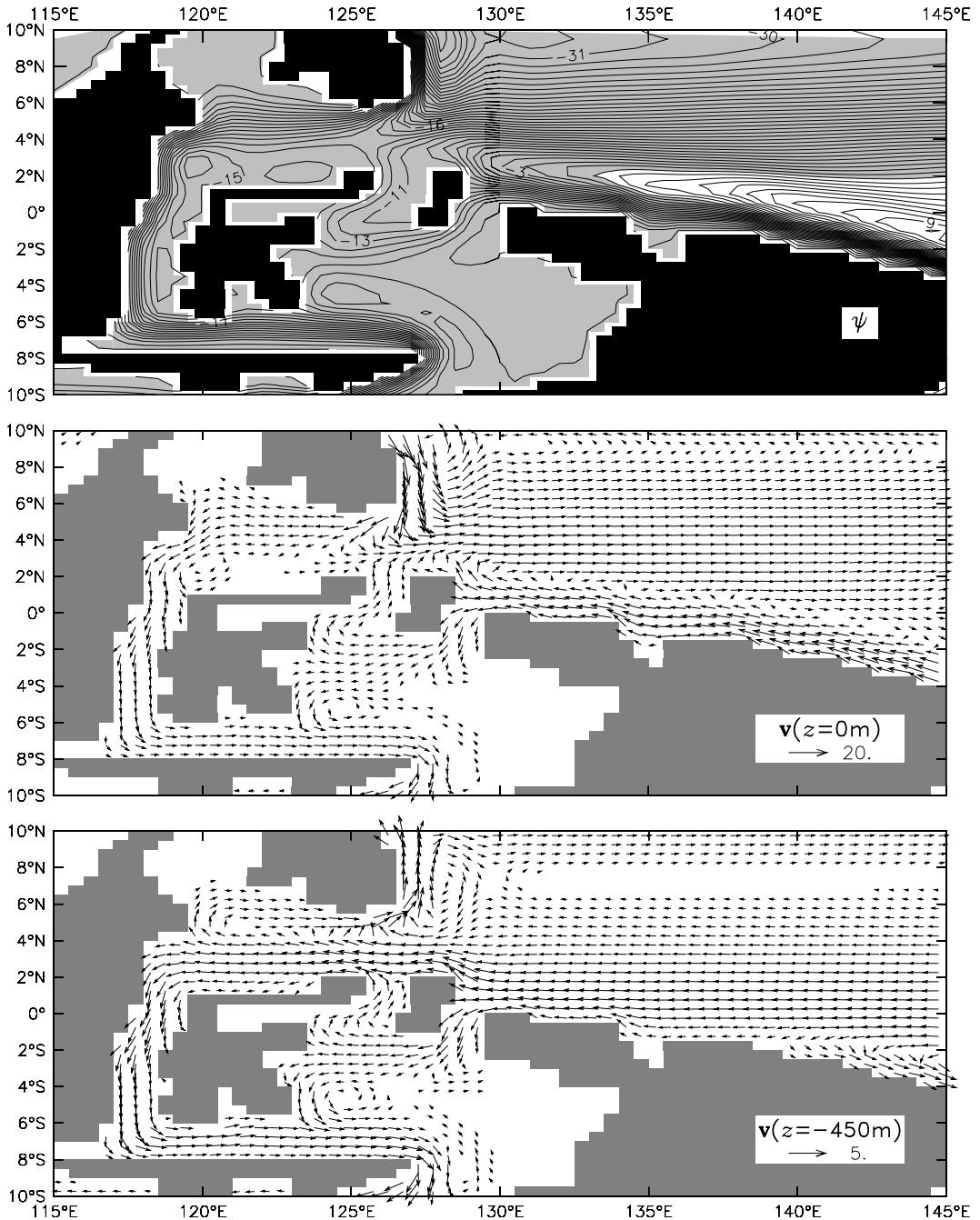


Fig. 8. Horizontal maps of the barotropic streamfunction  $\psi$  (top), and current vectors at the surface (middle) and at 450 m (bottom) from Solution D. In the top panel, the contour interval is 1 Sv. To illustrate weaker flows better, arrow lengths are proportional to the square root of the vector amplitudes, so that the unit of the calibration arrows is  $(\text{cm/s})^{\frac{1}{2}}$ .

then to the Timor Strait. Consistent with the observed IT (*e.g.* Talley and Sprintall, 2005; Gordon, 2005), the IT transport is split between southern (3.2 Sv) and northern (13.8 Sv) sources, which are mostly confined to the deep and shallow cores, respectively. Note that, contrary to observations, the flow along the eastern portion of New Guinea at 450 m is directed southeastward so that the IT is fed by an eastward flow near the equator rather than by the NGCUC. This model discrepancy is traceable to the unrealistic eastward flow south of 5°S in the interior ocean at that depth (Fig. 7), a result of the simplicity of the damping of Rossby waves in the LCS model.

To help understand why IT source waters come mostly from the northern hemisphere in Solution D, Fig. 9 plots the streamfunction  $\psi'$  from a run like Solution D but with closed Indonesian passages (Solution D'; top) and the difference streamfunction  $\Delta\psi = \psi - \psi'$  from Solution D – Solution D' (Solution  $\Delta D$ ; bottom). The fields split  $\psi$  into two parts:  $\psi'$  driven only by the Pacific winds, and  $\Delta\psi$  due only to the circulation around Australia. The  $\psi'$  field has anticlockwise and clockwise circulations in the Pacific interior, namely, the North and South Pacific Tropical Gyres, respectively; they are wind-driven Sverdrup circulations located between the Subtropical Gyres, somewhat modified by viscosity. Their western boundary currents converge near the latitude  $y_0$  where  $\psi' = 0$  in the interior ocean, which for Solution D is located about 2°N (top panel of Fig. 9); hence, the flow in the Sulawesi Sea is part of the North Pacific Tropical Gyre, with water from the Mindanao Current circulating anticlockwise around its perimeter. In contrast,  $\Delta\psi$  has westward flow along the northern coast of Sulawesi. The eastward branch of the Sulawesi Sea circulation in  $\psi'$  is almost strong enough to cancel the westward flow of  $\Delta\psi$  there, thereby ensuring that almost all the water in the Makassar Strait comes from the north (top panel of Fig. 8).

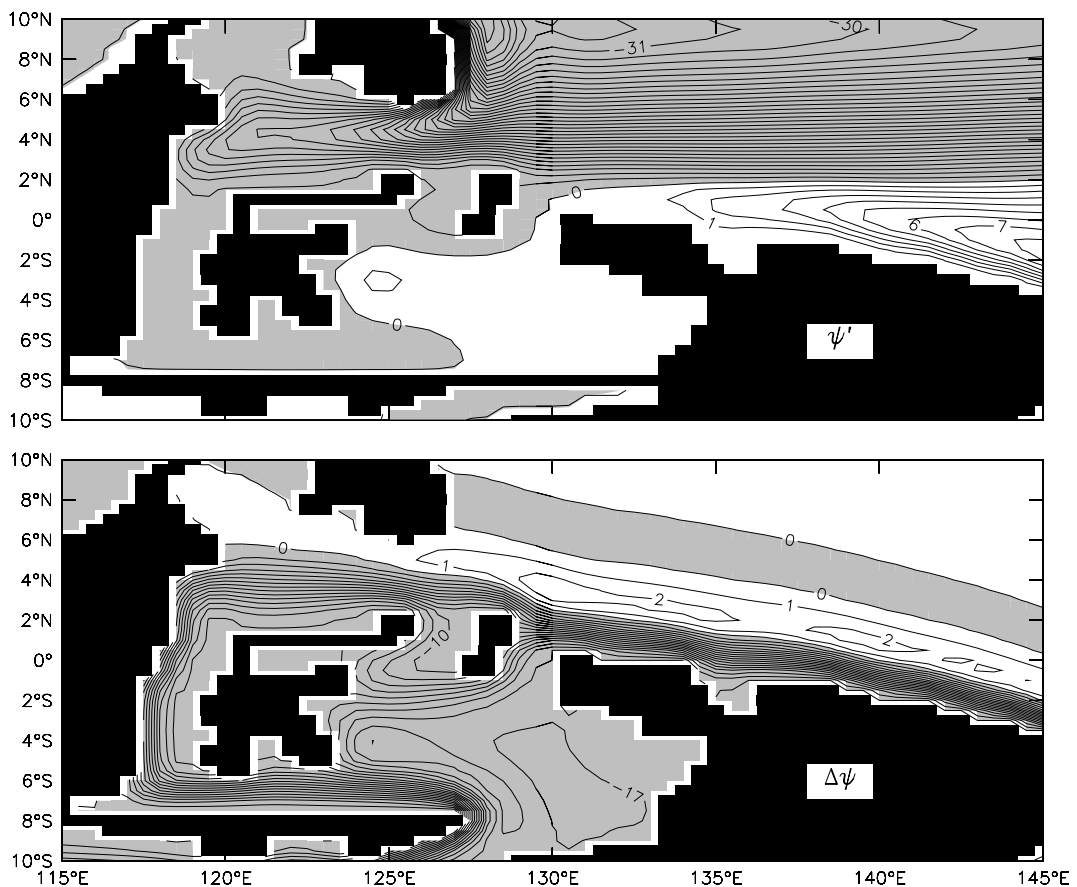


Fig. 9. Horizontal maps of the barotropic streamfunction  $\psi'$  (top) and  $\Delta\psi = \psi - \psi'$  (bottom) from Solutions D' and  $\Delta D$ , respectively. The contour interval is 1 Sv.

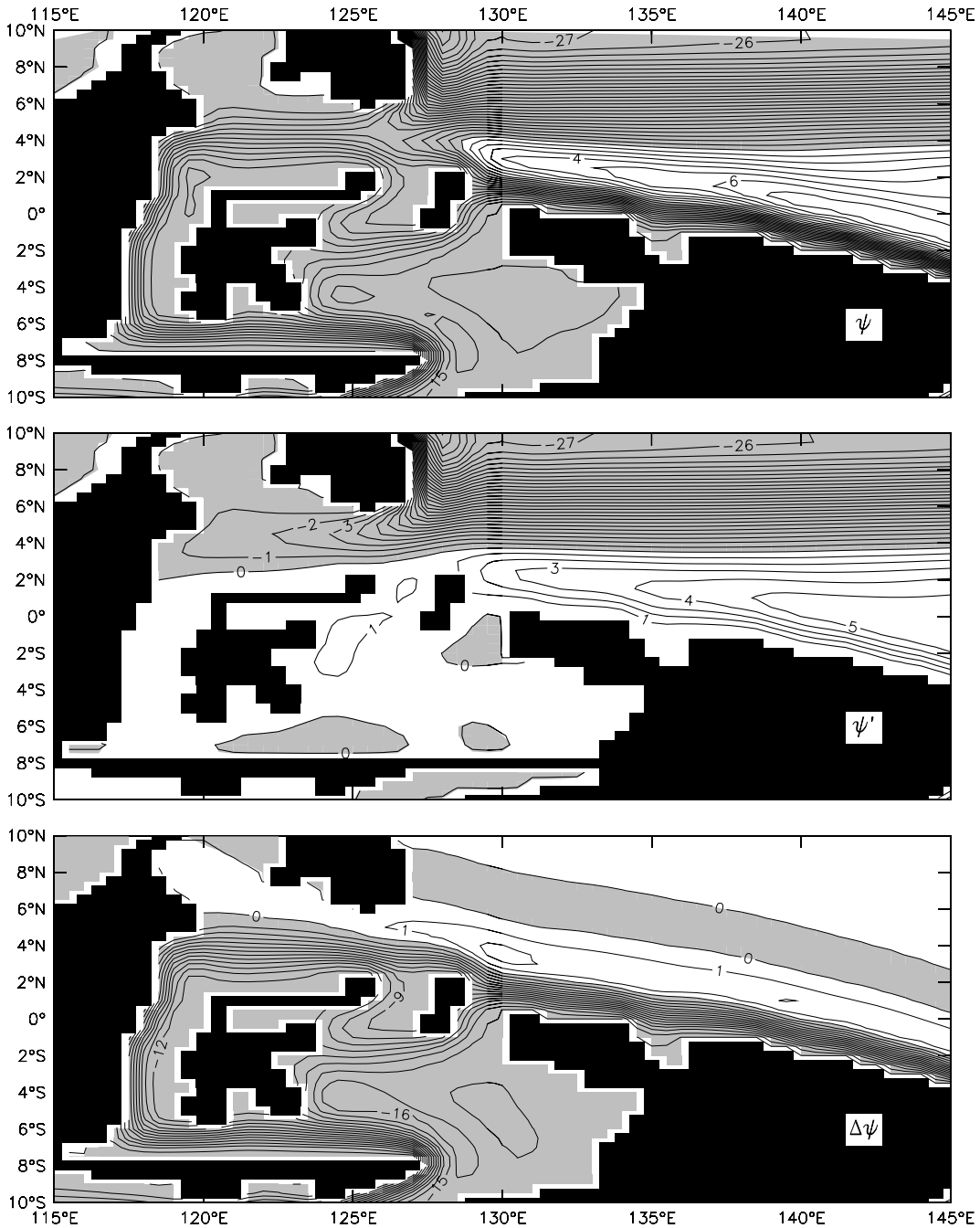


Fig. 10. Horizontal maps of the barotropic streamfunction  $\psi$  (top),  $\psi'$  (middle), and  $\Delta\psi$  (bottom) from Solutions E, E', and  $\Delta E$ , respectively, which are forced by ERA15, rather than HR, winds. The contour interval is 1 Sv.

To understand why the deep IT comes from the south, it is necessary to consider the vertical structure of the flows in Solutions D' and  $\Delta D$ . Recall that the baroclinic contributions tend to concentrate flows in the upper ocean. As a result, the flow fields of Solutions D' and  $\Delta D$  do *not* have the same vertical extent in the Indonesian Seas: in Solution D' currents are contained primarily within and above the thermocline [as for the North Equatorial Current (NEC) and North Equatorial Countercurrent (NECC) in Fig. 7], a consequence of its being significantly forced by nearby (local and western Pacific) winds, whereas in Solution  $\Delta D$  they

extend to intermediate depths. Only near the surface, then, is the anticlockwise circulation in the Sulawesi Sea in Solution D' strong enough to eliminate the westward flow of Solution  $\Delta D$ . Below the thermocline, where the currents of Solution D' are weak or absent, the IT source waters are necessarily from the south.

In general, whether the depth-integrated IT transport comes mostly from the north or the south is sensitive to the structure and strength of  $\psi'$  in the far-western Pacific and Sulawesi Sea, which depend on the nature of the wind forcing (Godfrey et al., 1993; Wajsowicz, 1993). A key factor is  $y_0$  relative to the southern latitude of the entrance to the Sulawesi Sea, which determines how much of the North and South Pacific Tropical Gyres are present in the Sulawesi Sea. Based on an analytic solution determined from Sverdrup dynamics using HR winds, Godfrey et al. (1993) noted that  $y_0$  was well north of New Guinea and concluded that all the IT must come from the south (see the discussion of their Fig. 3). Wajsowicz (1993) noted that Halmahera, which was neglected in the Godfrey et al. (1993) analysis, increases the likelihood of flow from the north, essentially by extending the entrance to the Sulawesi Sea from the equator to 2.5°N (although that simple interpretation is complicated by the fact that Halmahera is an island not connected to New Guinea). Other factors that can impact the IT source waters are the strength of viscosity, which sets the width of boundary currents, and the nonlinear overshoot of western boundary currents (Godfrey, 1996; Wajsowicz, 1993; Sections 4.2 and 5.2).

We tested the model's sensitivity to wind forcing, obtaining solutions like Solution D but forced by ERA15 (Solution E) and QuikSCAT winds. Fig. 10 plots  $\psi$ ,  $\psi'$ , and  $\Delta\psi$  for Solutions E, E', and  $\Delta E$ . The solutions are similar to their counterparts in Figs. 8 and 9, except that the anticlockwise circulation in the Sulawesi Sea in  $\psi'$  is weak. As a result, there is more water from the south (10.3 Sv) than the north (4.7 Sv). The reason for this difference is that  $y_0$  is located farther to the north (3.7°N), so that some of the South Pacific Tropical Gyre is present in the Sulawesi Sea. (There is no clockwise circulation south of  $y_0$  in the Sulawesi Sea because viscosity broadens the eastward and westward branches enough so that they overlap and, hence, cancel.) The QuikSCAT solution (not shown) is similar to Solution D except with even more flow from the north (14.2 Sv out of a total IT transport of 15.5 Sv), because  $y_0$  is located even farther south (1.45°N) thereby strengthening the anticlockwise circulation of  $\psi'$  within the Sulawesi Sea.

#### 4. Solutions to LOM

Solutions to the  $4\frac{1}{2}$ -layer model adjust to equilibrium in essentially the same way as the LCS model, with Solution  $\Delta LOM$  (Solution LOM – Solution LOM') spinning up via the radiation of baroclinic waves away from the Indonesian passages. Since they share this common dynamics, general features of the LCS difference solutions and Solution  $\Delta LOM$  are similar. On the other hand, because LOM is nonlinear and baroclinic waves are damped by different processes, there are obvious differences in the flow fields of the two models, with the LOM solutions tending to have a more complex structure.

##### 4.1. General features

To illustrate the steady-state response, Figs. 11 and 12 plot fields from Solution  $\Delta LOM$  averaged over the last 10 years of the integration, showing sea level  $\Delta d$  in Fig. 11, and transport/width vectors,  $\Delta(h_1\mathbf{v}_1 + h_2\mathbf{v}_2)$ ,  $\Delta(h_3\mathbf{v}_3)$ , and  $\Delta(h_4\mathbf{v}_4)$  (vectors) and across-interface velocities  $\Delta w_i$  at the tops of layers 3 and 4 (shading) in Fig. 12. We show the upper ocean transport field,  $\Delta(h_1\mathbf{v}_1 + h_2\mathbf{v}_2)$ , rather than  $\Delta(h_1\mathbf{v}_1)$  and  $\Delta(h_2\mathbf{v}_2)$  separately, since our focus is on currents below the thermocline; for convenience, we refer to the combination of layers 1 and 2 as “layer 1 + 2”. (The Subtropical Cells are well represented in the LOM solutions, but they are contained entirely within layers 1 and 2 and so are not visible in the layer 1 + 2 fields. As discussed by Lu et al. (1998) and Lee et al. (2002), the IT alters their structure so that more southern-hemisphere, thermocline water moves to the equator.)

As for Solution  $\Delta A$ ,  $\Delta d$  indicates a transfer of water from the Pacific to the Indian Ocean, with a sea-level rise concentrated in the southern Indian Ocean (Fig. 11). The change in thermocline depth,  $\Delta(h_1 + h_2)$  (not shown), has a very similar structure to  $\Delta d$  with  $\Delta(h_1 + h_2) \approx 300\Delta d$ ; thus, the IT acts to deepen the thermocline by more than 100 m off Australia. The interior flow fields in both basins are also similar, with generally eastward flow across the southern Indian Ocean in layer 1 + 2 overlying westward flow in layer 3, and the reverse for the Pacific Ocean (panels a and b of Fig. 12; geostrophic streamlines for the layer 1 flow in Fig. 11).

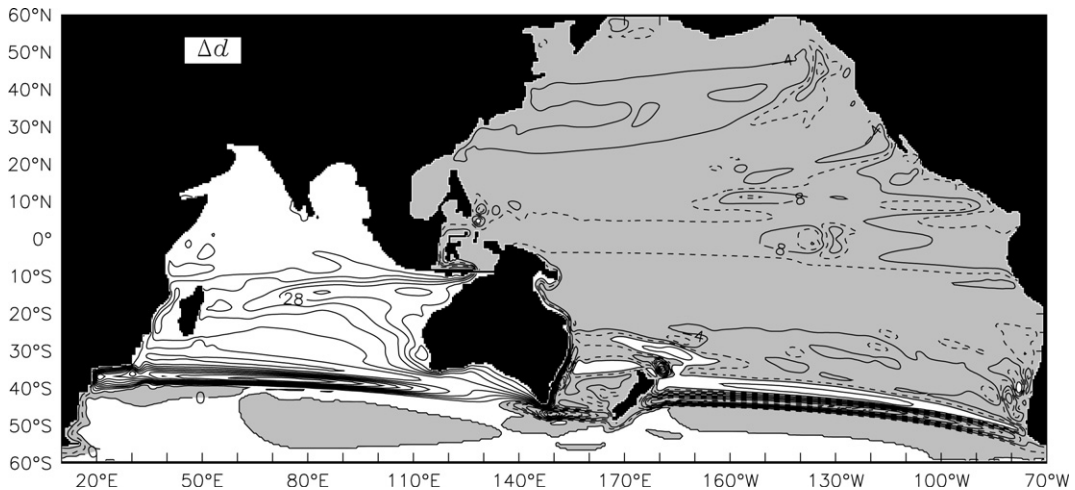


Fig. 11. Horizontal map of the total sea level  $\Delta d$  from Solution  $\Delta$ LOM. Contour intervals are 4 cm (solid) and 2 cm (dashed). Cyclic boundary conditions are applied along  $60^\circ\text{W}/20^\circ\text{E}$ , and the region from  $70^\circ\text{W}$  to  $60^\circ\text{W}$  is plotted at the left hand side of the figure.

A striking difference between the two solutions is the curved bands of  $\Delta d$  and currents across the basin from  $35^\circ\text{S}$  to  $50^\circ\text{S}$  in Solution  $\Delta$ LOM, which are absent in Solution  $\Delta$ A. They correspond to shifts in the position of the model's ACC due to the IT (a nonlinear process), with the current shifting southward (northward) in the Indian (Pacific) Ocean (Fig. 12); as a result, the difference fields in each layer have an eastward anomalous current located just north of a westward one in the Indian Ocean and vice versa in the Pacific. There is also a net change in the ACC transport in each sector, with an increase in the Indian Ocean (10.3 Sv) and a decrease in the Pacific Ocean ( $-2.2$  Sv), their difference accounting for the net IT transport (12.5 Sv). We note that in Solution LOM' without the IT, the average ACC transport is 34.6 Sv, much weaker than the observed value because LOM lacks a barotropic response.

The model ACC is narrower and located farther north than the observed one. It is generated by northward Ekman drift in the Southern Ocean, which forces the upper four layers to their minimum thicknesses south of the ACC, that is, all four layers effectively outcrop there (Appendix A). The ACC extends from the southern tips of land masses, where Rossby waves can first radiate westward, thereby replacing Ekman drift with a Sverdrup flow. The northward bending of the ACC path to the west in each basin likely results from nonlinear dynamics similar to those discussed in Rhines and Young (1982) and Luyten et al. (1983), in which higher-order baroclinic Rossby waves propagate along characteristic curves rather than due westward.

Regions of significant transfer across the tops of layers 3 and 4 are indicated by shading in Figs. 12b and 12c, respectively. The existence of localized regions of upwelling and downwelling is very different from the relatively uniform diffusion in the LCS model, and this difference accounts for most of the differences in the baroclinic circulations between the two models.

In the Indian ocean, there is anomalous downwelling from layer 2 to layer 3 in the western ocean from  $5^\circ\text{S}$  to  $10^\circ\text{S}$  and in a wedge-shaped region extending from Australia (Fig. 12b); it occurs because there is upwelling in these regions in Solution LOM', due to both  $h_1$  and  $h_2$  attaining their minimum thicknesses (40 m; Appendix A), which is absent in Solution LOM. There is also a region of strengthened subduction from layer 2 to layer 3 in Solution LOM, south of  $32^\circ\text{S}$  in the southeastern Indian Ocean and south of Australia, where  $h_1$  and  $h_2$  are deeper than their allowed maximum (80 m). Finally, there is also weak, anomalous downwelling from layer 3 to layer 4 throughout much of the basin due to the model's internal diffusion (visible in Fig. 12c only in the southern Indian Ocean).

In the Pacific Ocean, there is strengthened upwelling in Solution  $\Delta$ LOM from layer 3 to layer 2 off South America, within, and extending westward from, the Costa Rica dome, and along Mexico (Fig. 12b). There is upwelling from layer 4 to layer 3 in the Subpolar Gyre (SPG) driven by the Ekman suction there (Fig. 12c), and weak upwelling in the northeast subtropics and the South Pacific (too weak to be visible in Fig. 12c). Finally, there are across-layer transfers within the ACC, where layer thicknesses vary considerably.

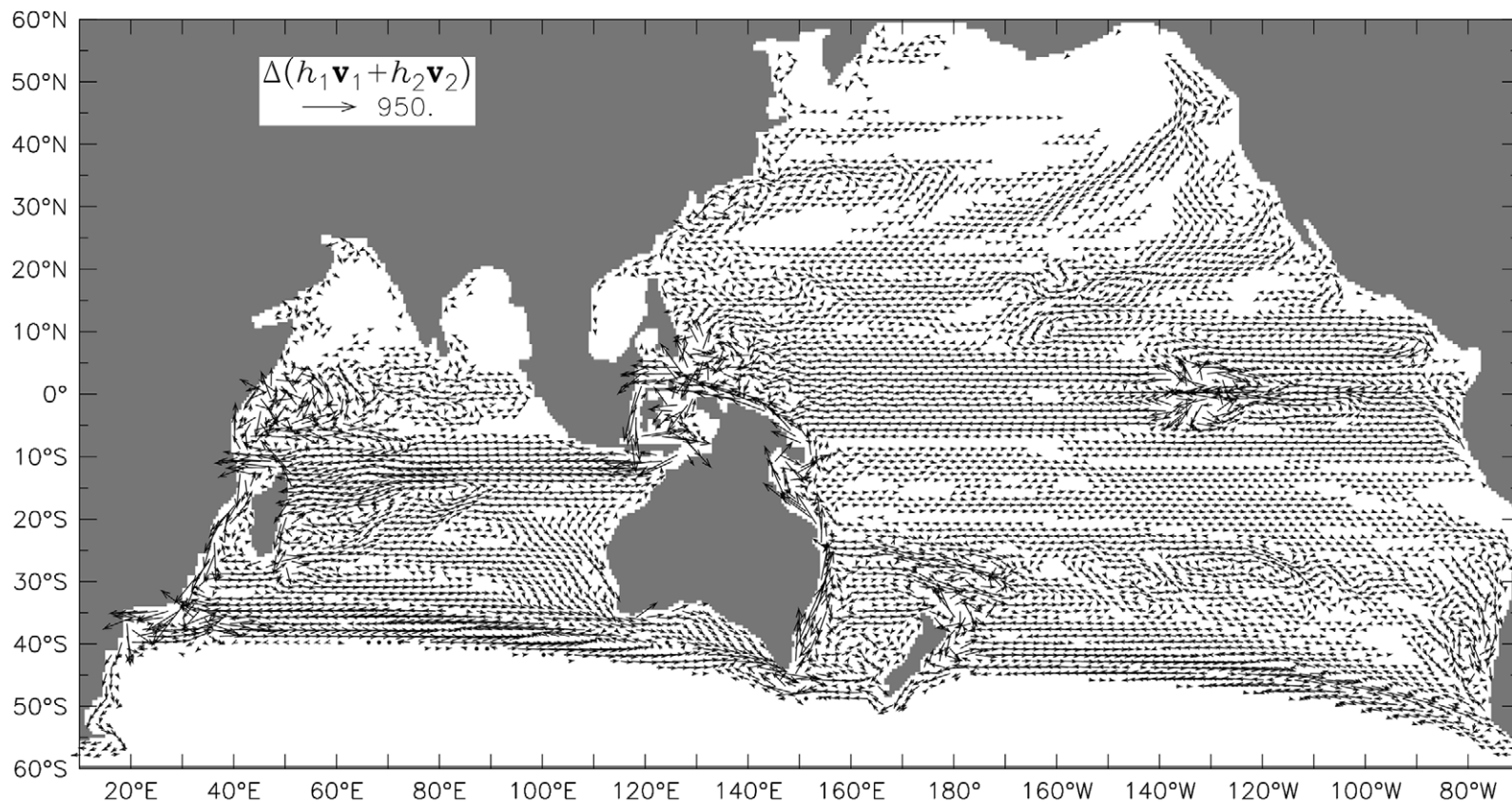


Fig. 12a. Horizontal map of transport/width vectors for layer 1 + 2 from Solution  $\Delta$ LOM. To illustrate weaker flows better, arrow lengths are proportional to the square root of the vector amplitudes, so that the unit of the calibration arrow is  $(\text{cm}^2/\text{s})^{\frac{1}{2}}$ . Cyclic boundary conditions are applied along 60°W/20°E, and the region from 70°W to 60°W is plotted at the left hand side of the figure.

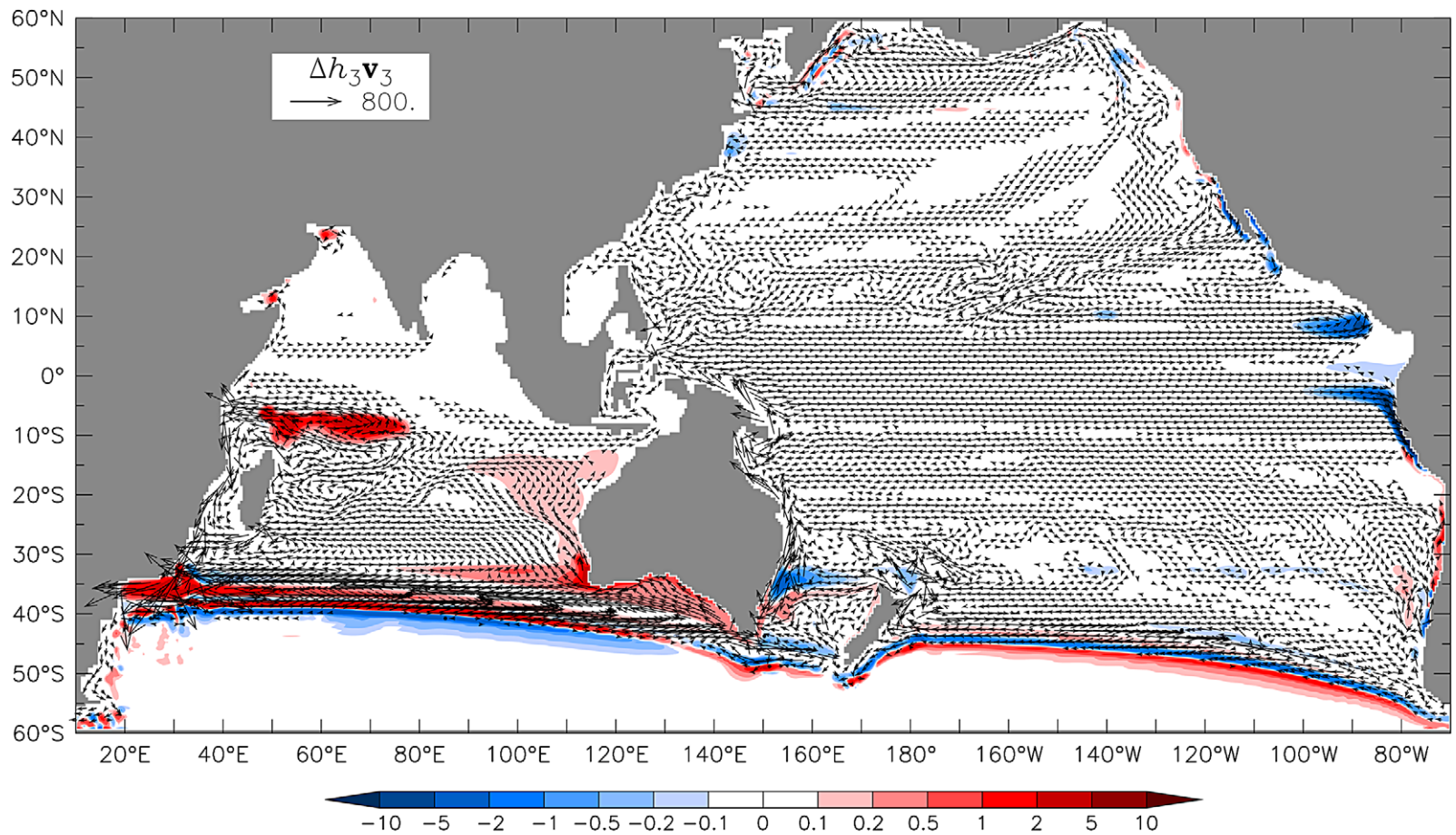


Fig. 12b. As in Fig. 12a, except for layer 3. Also shown are across-interface velocity anomalies at the bottom of layer 2, with negative values indicating a transfer of water from layer 3 into layer 2. The unit for the color bar is  $10^{-4}$  cm/s.

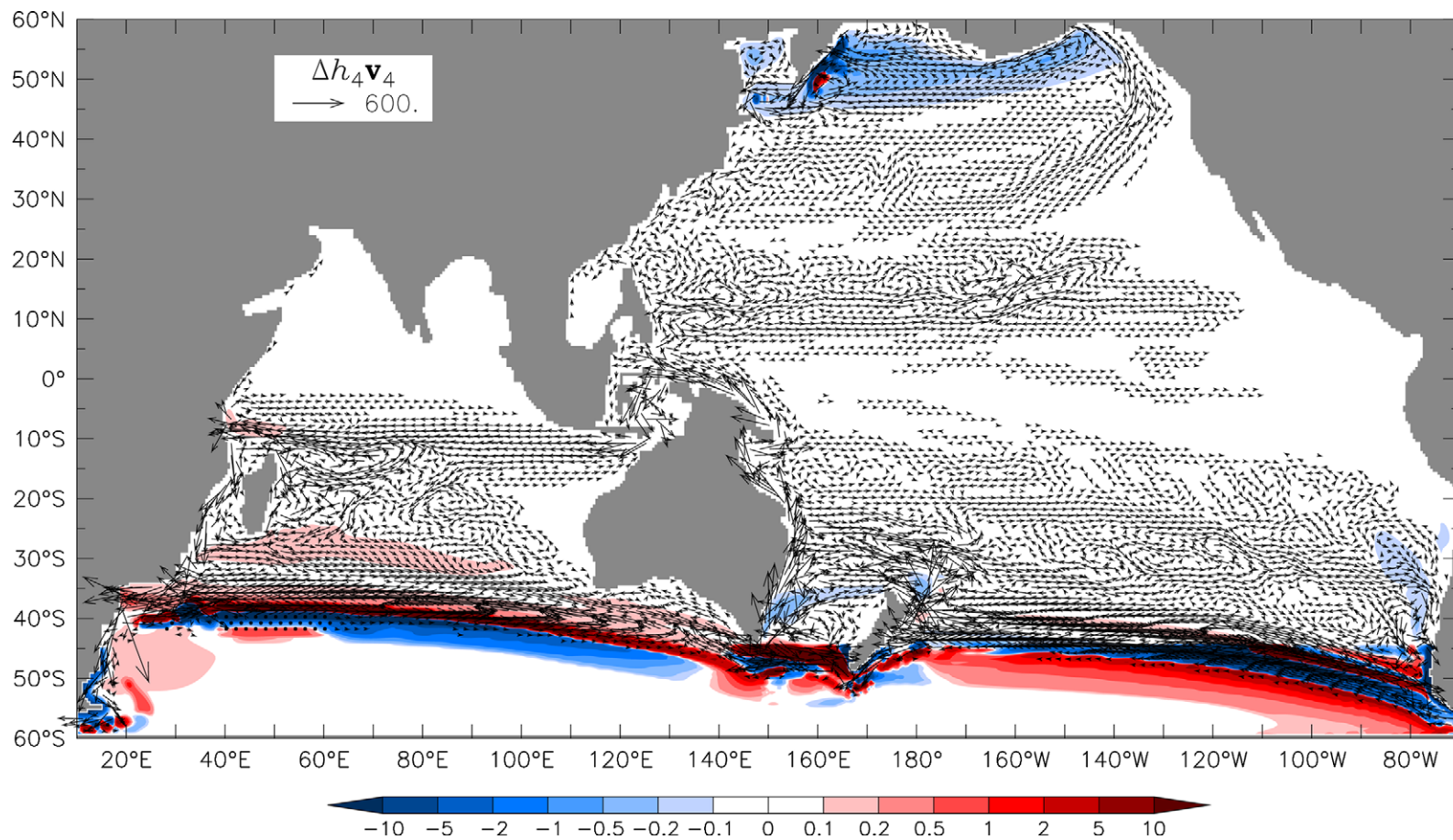


Fig. 12c. As in Fig. 12a, except for layer 4. Also shown are across-interface velocity anomalies at the bottom of layer 3, with negative values indicating a transfer of water from layer 4 into layer 3. The unit for the color bar is  $10^{-5}$  cm/s.

4.2. Indonesian Seas

The column in Table 2 labelled IT describes the vertical structure of the flow through the Indonesian passages, listing the total throughflow transport (−12.5 Sv) as well as the transports in each layer, and Fig. 13 shows the circulation within the Indonesian Seas for Solution LOM. Water flows into the Indian Ocean in layers 1, 2, and 4 (−6.8, −3.4, and −2.7 Sv, respectively), but, for the reasons discussed later in Section

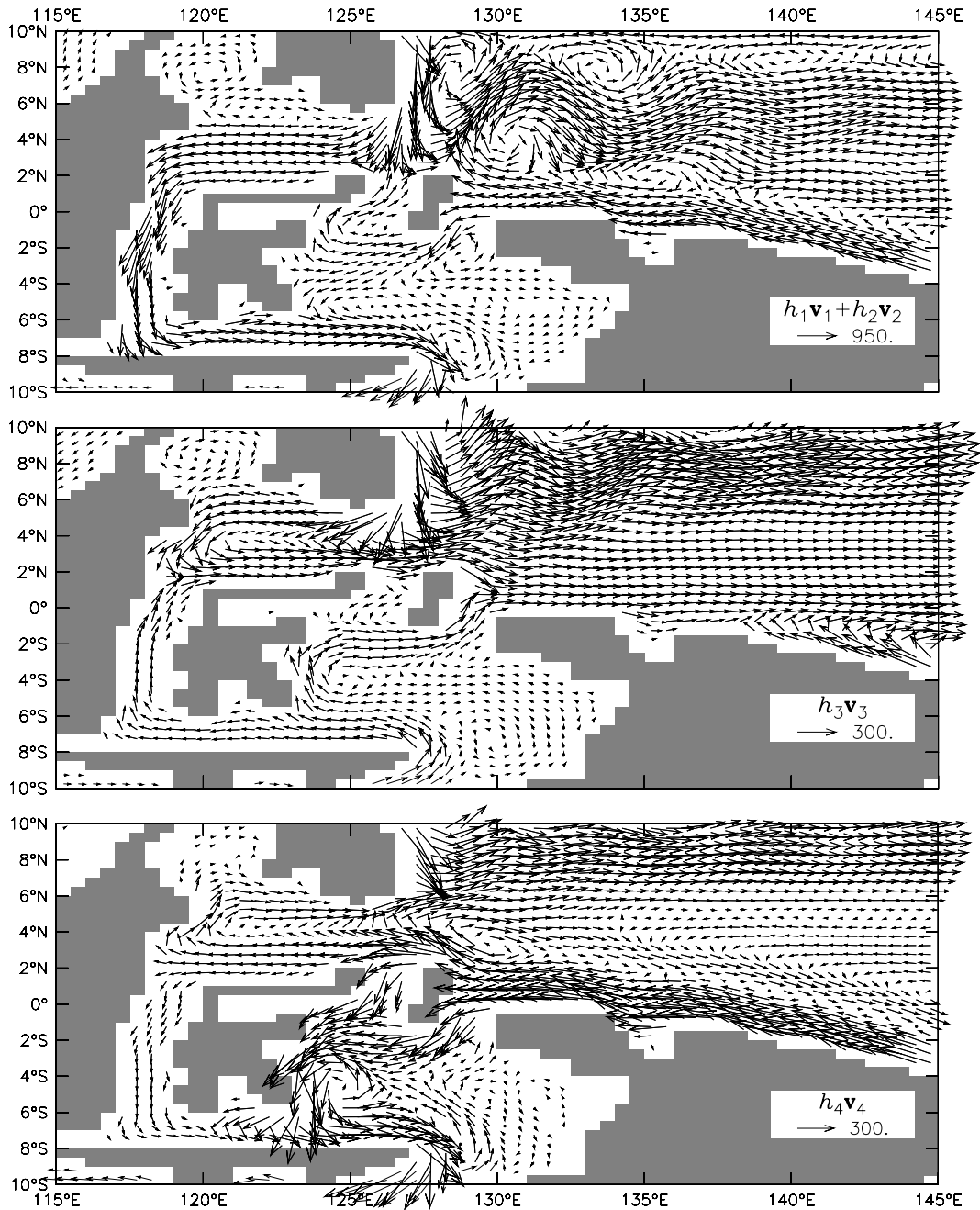


Fig. 13. Horizontal maps of transport/width vectors in the Indonesian Seas for layer 1 + 2 (top), layer 3 (middle), and layer 4 (bottom) from Solution LOM. To illustrate weaker flows better, arrow lengths are proportional to the square root of the vector amplitudes, so that the unit of the calibration arrows is  $(\text{cm}^2/\text{s})^{\frac{1}{2}}$ .

4.4.2, there is a small return transport into the Pacific in layer 3 (+0.4 Sv). Note that the transport in layer 4 is substantial, consistent with observed estimates for the deep core (Molcard et al., 1996; Talley and Sprintall, 2005; Gordon, 2005). The total transport is somewhat weaker than the Island-Rule estimate for ERA15 winds (15 Sv). Recall that the Island Rule is based on Sverdrup dynamics (Godfrey, 1989): since the total transport field ( $\sum_{i=1}^4 h_i \mathbf{v}_i$ ) is unaffected by diffusion and there is no bottom topography, the decrease must happen because of the existence of viscosity and momentum advection in LOM (Wajsowicz, 1995; Godfrey, 1996).

In Solution  $\Delta$ LOM, the layer 1 + 2 flow enters the Indonesian passages directly from the south (Fig. 12a). In contrast, in Solution LOM most of the southern-hemisphere water retroflects to join the NECC and EUC (10.4 Sv out of 13.7 Sv; top panel of Fig. 13); the rest flows into the Banda Sea through the Halmahera Sea (3.3 Sv), with more than half of it returning northward through the Maluku Strait (1.9 Sv). These features are very similar to the near-surface flow field of Solution D (middle panel of Fig. 8). Consistent with observations and other models, then, the amount of near-surface, southern-hemisphere water that participates in the IT is small (1.4 Sv out of 10.2 Sv).

It is noteworthy that the near-surface flow is mostly from the north, since it is mostly from the south in the corresponding LCS solution forced by ERA15 winds (Solution E; top panel of Fig. 10). This difference between solutions results from the nonlinearities in LOM. One nonlinear effect is the tendency for potential vorticity to be conserved, which requires that the surface New Guinea Coastal Current (NGCC) retroflects as it crosses the equator (Godfrey et al., 1993). Another is the overshoot of the Mindanao Current south of the southern tip of the Philippines, which “blocks” the flow of surface NGCC water into the Sulawesi Sea.

Consistent with the LCS solutions and observations, the IT source waters in layer 4 come from the southern-hemisphere (bottom panel of Fig. 13). Otherwise, the layer 4 flow within the Indonesian Seas is quite different between the solutions, with most of the IT flowing to the Timor Strait through the Banda Sea in Solution LOM, rather than the Makassar Strait as in Solution D (compare bottom panels of Figs. 8 and 13). One reason for this difference is the different structures of the flow fields in the interior Pacific: the stronger eastward current east of the Philippines in Solution LOM (see Section 4.4.3) drives a stronger northward current in the Makassar Strait, thereby weakening the overall southward flow there; in addition, the westward flow that enters the Indonesian Seas occurs via the narrow NGCUC in Solution LOM, rather than as an equatorial current in Solution D, thereby allowing more water to bend southward around Halmahera. Another reason is the existence of southward flow in the Maluku Strait (west of Halmahera), which is northward in Solution D. This difference must result from nonlinear interactions between layer 4 and the overlying layers: in a linear version of LOM without across-layer transfer ( $w_i = 0$ ), eastward flow toward Sulawesi in subsurface layers must bifurcate, so that the flow in Maluku Strait is northward.

### 4.3. Indian Ocean

The near-surface circulations in the interior of the southern Indian Ocean have a more complex structure than the surface flow in Solution  $\Delta$ A (compare Figs. 11 and 12 with Fig. 3). Specifically, eastward flow across the basin in layer 1 + 2 is split into three branches: one near and south of 30°S, another near 25°S, and a third that first flows northeastward into the tropics before bending to the south in the eastern ocean. The latter flow is associated with regions of strengthened downwelling (within the lighter red area north of 20°S in Fig. 12b), with currents circulating around and extending westward from them. Consistent with this idea, note that the layer 1 + 2 and layer 3 circulations tend to mirror each other there, an inherent property of flows driven by across-layer transfer. The current near 25°S extends to the subduction region south of 32°S in the eastern ocean. These two currents correspond to the broad, southeastward surface flow in Solution  $\Delta$ A (Fig. 3), although modified considerably by different mixing processes. A similar circulation exists in the Hirst and Godfrey (1993) and COCO solutions, except that the currents converge to the southwest corner of Australia (see Section 5.3). The cause of the current south of 30°S is not clear, but it appears to be linked to the shift in the position of the ACC and to the strengthened subduction south of Australia.

Because of convergences and divergences driven by the interior circulation, the currents around the perimeter of the southern Indian Ocean change their vertical structure markedly away from the Indonesian passages (Table 2). Even by 90°E, the layer 3 flow is directed westward, a result of the influx of layer 3 water from the subduction region south of 32°S (Fig. 12b), and at 30°S most of the transport occurs in layer 3. Note that the

transport changes do not vary monotonically away from the Indonesian passages, due to the complexity of the interior circulations. Indeed, for the zonal transports across the basin, especially at 50°E, it is difficult to define clearly the edges of the current.

#### 4.4. Pacific Ocean

##### 4.4.1. South Pacific

The structure of the South Pacific inflow along the Australian coast at 40°S is spread throughout all four layers (Table 2). The inflow is thus much deeper than the IT outflow, owing to the downward, across-layer transfers in the Indian Ocean and south of Australia noted above. As the IT-associated western boundary current flows northward, its transport remains roughly uniformly distributed among the layers to 5°S. Only north of that latitude does its vertical structure begin to adjust to that of the IT, a rapid change similar to that in the LCS model (Fig. 5).

The reason for the abrupt change is that the interior baroclinic flows, which drain water from the western boundary current in layer 3 and supply water to it in layer 1 + 2, are largely confined north of 5°S (Figs. 12a and 12b). Indeed, the difference currents, although visible in Fig. 12, are weak in the South Pacific south of 5–10°S in all the layers, indicating that the IT has little impact on the extratropical, South Pacific circulation away from the western boundary currents.

In Solution LOM, the East Australian Current (EAC) is directed southward in all layers from the bifurcation latitude of the SEC in each layer to the latitude of the northern tip of New Zealand at 35°S (Fig. 14). Thus, IT-associated water cannot flow directly northward into the tropics along the Australian coast, as suggested by Solution  $\Delta$ LOM. Instead, it must first recirculate in the South Pacific STG, arriving at the coast north of the bifurcation latitude in each layer. As a result, IT-associated water enters the South Pacific east of New Zealand, bending northward from the ACC across the width of the basin. In fact, almost all the IT-associated water first flows northward along the southeastern coast of Australia (11.9 Sv); however, it bends eastward at 36°S, flows southward along the east coast of New Zealand, and rejoins the northernmost portion of the ACC before entering the interior ocean. This pathway does not exist in nature, as the observed EAC continues to flow southward south of 36°S and the overall Tasman-Sea transport is southward (Ridgway, 2005, personal communication). Its likely cause in Solution LOM is the ACC being too narrow and located too far north, a consequence of all four of its active layers outcropping in the Southern Ocean (Appen-

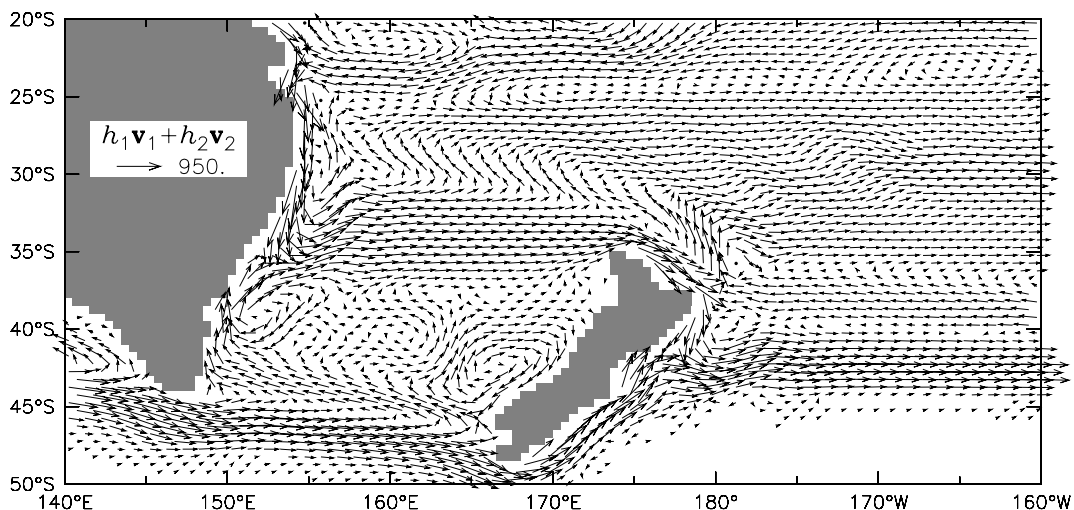


Fig. 14. Horizontal map of transport/width vectors in the Southwest Pacific for layer 1 + 2 from Solution LOM. To illustrate weaker flows better, arrow lengths are proportional to the square root of the vector amplitudes, so that the unit of the calibration arrow is  $(\text{cm}^2/\text{s})^{1/2}$ . The flow fields in layers 3 and 4 (not shown) are very similar.

dix A). A similar pathway exists in Solution COCO (see Section 5.4.1). Tilburg et al. (2001) also reported northward transport across the Tasman Sea in solutions to nonlinear  $5\frac{1}{2}$ -layer and 6-layer, flat-bottom models, attributing it either to layer outcropping or to the IT being too strong.

As noted above, the IT has little impact on the South Pacific STG away from the western boundary (Fig. 12). To allow for the northward IT transport (12.5 Sv), then, the northward EAC anomaly in Solution  $\Delta$ LOM shifts the SEC bifurcation latitude southward in each layer so that more of the SEC bends equatorward at the Australian coast. Specifically, the bifurcation latitudes in Solution LOM' are 16.1°S, 15.1°S, 14.9°S, and 14.9°S in layers 1, 2, 3 and 4, respectively, whereas in Solution LOM they are 18.1°S, 16.6°S, 17.7°S, and 23.0°S. Note that the shift increases with depth, a result of the background currents in Solution LOM' weakening with depth. A similar southward shift occurs in COCO (see the discussion of Fig. 22).

#### 4.4.2. Tropical Pacific

In the tropical Pacific, there are generally westward currents in layer 1 + 2 overlying eastward flow in layer 3 (Fig. 12). The layer 1 + 2 flow is split into a number of zonal jets in the eastern ocean by the presence of the EUC within layer 2. The curious feature on the equator near 130°W indicates a westward shift in the western edge of the equatorial upwelling region, a result of more layer 1 than layer 2 water being drained from the Pacific by the IT; it represents an expansion (strengthening) of the cold tongue due to the IT, a property noted in several previous studies (Hirst and Godfrey, 1993, 1994; Lee et al., 2002).

The interior circulation is closed by strengthened upwelling from layer 3 to layer 2 off South America and near the Costa Rica dome (Fig. 12b). The strengthened upwelling is, in turn, forced by the draining of layer 1 + 2 water from the basin by the IT, which thins both  $h_1$  and  $h_2$  to their minimum allowed thicknesses in the upwelling regions. Note that there is an anticyclonic circulation around the Costa Rica dome in layer 3 and a reverse circulation in layer 1 + 2, consistent with the properties of an upwelling-driven “beta plume” (Spall, 2000; McCreary et al., 2002).

The near-equatorial, eastward flows in layer 3 are the model's TJs. Interestingly, they are *absent* in Solution LOM': in that solution, the only appreciable, tropical flow crosses the basin south of about 5°S to supply water for coastal upwelling south of 12°S. A similar result was reported by McCreary et al. (2002), leading them to conclude that drainage of upper-layer water by the IT was necessary for the existence of TJs. As we shall see in Section 5, our COCO solutions suggest a different conclusion.

The existence of the Pacific's TJ circulation is the reason why the IT is reversed in layer 3: in Solution LOM (middle panel of Fig. 13), water from the Indian Ocean flows into the Pacific north of 2°N through the Makassar Strait and Sulawesi Sea and near the equator through the Halmahera Sea, both flows eventually joining the northern TJ (Fig. 12b). As for the LCS model, then, the property that the IT is divided into surface (layer 1 + 2) and deep (layer 4) branches results from basin-scale baroclinic processes throughout the tropical Pacific. This idea is confirmed in a test solution with stronger vertical diffusion (velocity  $w_{mi}$  defined in Appendix A), for which the layer 3 flow is directed from the Pacific to Indian Ocean. Interestingly, there is also a reverse flow in the density range of thermostad water in a solution to the OFES model, a high-resolution (10 km), global OGCM being run on the Earth Simulator computer in Japan, but the reversal cannot be definitively linked to currents in the eastern Pacific (Masumoto et al., 2004; Potemra, 1999, private communication).

In both Solutions  $\Delta$ LOM and LOM, layer 3 water flows northward along New Guinea to the equator (Figs. 12 and 13). In striking contrast, in Solution LOM' (not shown) layer 3 water from the North Pacific flows southward along the New Guinea coast to 9°S, and then flows across the basin to supply some of the water that upwells along Peru south of 12°S. As a result, northern hemisphere water fills the near-equatorial ocean in layer 3. McCreary and Lu (2001) obtained a similar result (see the discussion of their Fig. 5), concluding that the IT is the reason why observed thermostad water is primarily of southern-hemisphere origin. The layer 4 circulation is negligible everywhere near the equator in Solution LOM' (not shown), so that the northern- and southern-hemisphere circulations are completely separate in that layer. Thus, the IT is the reason that AAIW (layer 4) water crosses the equator to flow into the northern ocean in Solution LOM. As we shall see, analogous (albeit weaker) changes occur in Solution COCO' (Section 5.4.2).

#### 4.4.3. North Pacific

Most of the layer 4 flow exits the Pacific basin via the IT (2.7 Sv out of 3.5 Sv; Fig. 12c). The rest (0.8 Sv) continues to flow into the North Pacific, eventually entering the SPG. Remarkably, the northward flow is disrupted by currents generated by the Hawaiian Islands. In Solution LOM (and LOM'), these currents consist of the eastward-flowing Hawaii Lee Countercurrent (HLCC; Qiu et al., 1997; Flament et al., 1998; Xie et al., 2001; Yu et al., 2003) in layer 1, and westward-flowing currents with flanking eastward flows in the deeper layers (Fig. 15). Hawaii is *not* a land mass in LOM, so all the structure arises from the forcing by ERA15 winds, which *does* include effects of the islands. The layer 1 + 2 currents are therefore driven entirely by orographically-induced wind curl that is strong enough to force upwelling of layer 2 water into layer 1; these currents are unstable, and the resulting eddy field drives the flows in layers 3 and 4. To move northward, then, layer 4 water must first flow eastward in the current near 8°S that extends from the western boundary to Hawaii and then return to the western ocean in the westward return flow near 15°N, although individual water parcels can circumvent this long, mean pathway within the eddies.

In Solution  $\Delta$ LOM, layer 4 water flows into the subpolar ocean as a narrow current through a baroclinic “window” in the northeast corner of the basin (Pedlosky, 1984; Lu et al., 1998; McCreary and Lu, 2001). This deep across-gyre exchange is driven by strengthened upwelling in the subpolar ocean (blue area north of 40°N in Fig. 12c): with open passages, the upper three layers are somewhat thinner, which allows  $h_1$ ,  $h_2$ , and  $h_3$  to attain their minimum thicknesses more readily, thereby strengthening the upwelling. Water upwelled from layer 4 recirculates in the subpolar ocean within layer 3, and eventually upwells into layer 1 + 2 (Fig. 12b). Note that there is southward flow through the window in both layers 1 + 2 and 3 (just north of 40°N). When the contributions of the three upper layers are summed (*i.e.*, a superposition of Figs. 12a and 12b), the return flow is a mirror image of the layer 4 flow so that there is no net transport through the window, a property inherent in its basic dynamics (Pedlosky, 1984).

In fact, the aforementioned window flow does not represent actual pathways of layer 4 water in Solution LOM. The reason is that the difference field must be added to a double-gyre circulation [the deep parts of the Subtropical (STG) and Subpolar (SPG) gyres] present in Solution LOM', for which the flow around its perimeter is everywhere southward and strong enough to reverse the northeastward window circulation in Solution  $\Delta$ LOM. Thus, in Solution LOM layer 4 water enters the SPG as it flows eastward across the basin between the two gyres (Fig. 15; Endoh et al., 2004). In contrast, the layer 4 perimeter flow remained northward in the McCreary and Lu (2001) solution with open passages. This difference happens because McCreary and Lu (2001) did not allow IT outflow in layer 4, so that much more of the inflow (3.5 Sv) had to upwell in the

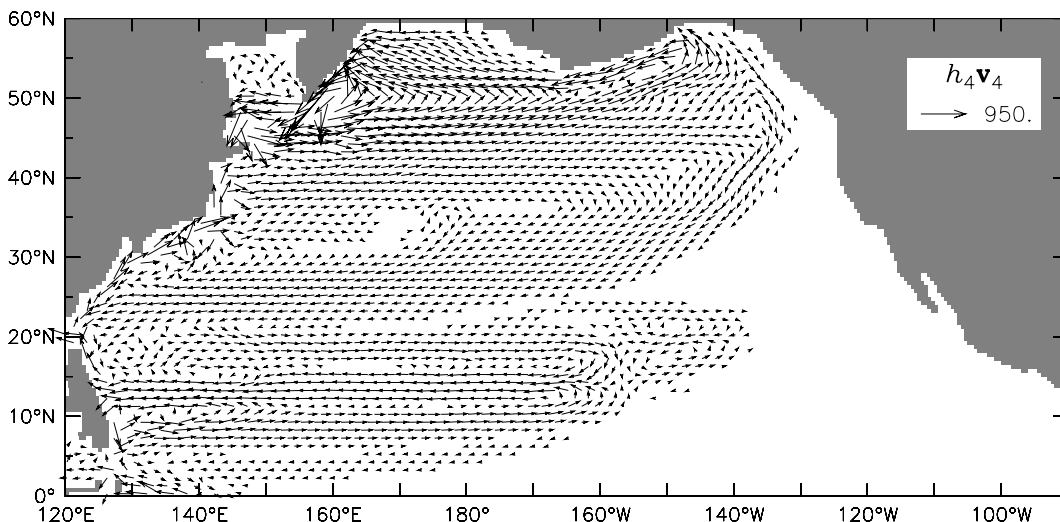


Fig. 15. Horizontal map of transport/width vectors in the North Pacific for layer 4 from Solution LOM. To illustrate weaker flows better, arrow lengths are proportional to the square root of the vector amplitudes, so that the unit of the calibration arrow is  $(\text{cm}^2/\text{s})^{\frac{1}{2}}$ .

SPG; consequently, the IT-associated flow was strong enough to reverse the southward perimeter flow in their corresponding solution with closed passages.

Finally, the IT also impacts coastal upwelling off Baja California and California. In Solution  $\Delta\text{LOM}$ , there are pairs of currents, oppositely directed in layers 1 + 2 and 3, that extend from the North American coast to Hawaii, which result from a strengthening and southward shift of the coastal upwelling there (Figs. 12a and 12b).

## 5. Solutions to COCO

Solution  $\Delta\text{COCO}$  (Solution COCO – Solution COCO') contains many of the features of the preceding solutions, as well as notable differences. In order to compare solutions more readily to their LOM counterparts, we define analogous layers by density bands from the surface to  $\rho_2 = 26.5 \sigma_\theta$  (layer 1 + 2),  $\rho_2$  to  $\rho_3 = 27.0 \sigma_\theta$  (layer 3), and  $\rho_3$  to  $\rho_4 = 27.4 \sigma_\theta$  (layer 4), which correspond to surface-plus-thermocline, subthermocline (thermostad), and upper-intermediate (AAIW) waters, respectively. This layer separation is also physically reasonable since these water masses do exist in COCO, but the layers are not as distinct as they are in LOM, a consequence of COCO having stronger internal diffusion.

### 5.1. General features

Figs. 16–18 plot the barotropic streamfunction  $\Delta\psi$ , sea level  $\Delta d$ , and transport/width vectors for the three density layers. Consistent with the  $n = 0$  response of the LCS model (top panel of Fig. 2) and previous GCM studies (e.g. Hirst and Godfrey, 1993; Lee et al., 2002),  $\Delta\psi$  forms an anticlockwise loop around the southern Indian Ocean and Australia closed by a northward current along the east coast of Australia (Fig. 16). Note that  $\Delta\psi$  is present in the interiors of the Pacific, Indian, and Southern Oceans, owing to variable bottom topography. As for Solutions  $\Delta\text{A}$  and  $\Delta\text{LOM}$  (Figs. 3 and 11),  $\Delta d$  extends prominently into the interiors of both basins, with positive values in the Indian Ocean mostly south of  $y_a$  and negative values in the Pacific (Fig. 17), and with the large-scale surface and subsurface currents tending to be oppositely directed (Fig. 18).

In contrast to Solution  $\Delta\text{LOM}$ , there are no basin-wide, recirculation bands corresponding to shifts in the position of the ACC, because the ACC is broader in COCO than in LOM (compare Figs. 18 and 12). There is, however, a near-surface cyclonic circulation in  $\Delta d$  in the South Pacific that extends from 120°W to Australia, and a zonal “dipole” in  $\Delta\psi$  from the dateline to 120°W (Figs. 16 and 17). Both features appear to be linked to a region of shallow bottom topography from 140°W to 160°W. They are probably generated by a northward

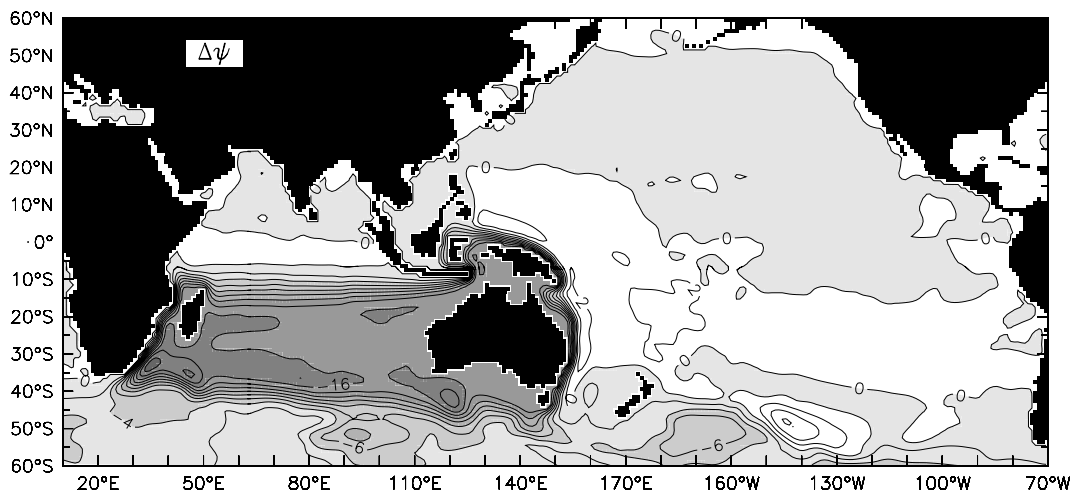


Fig. 16. Horizontal map of the barotropic streamfunction  $\Delta\psi$  from Solution  $\Delta\text{COCO}$ . The contour interval is 2 Sv, and negative values are shaded.

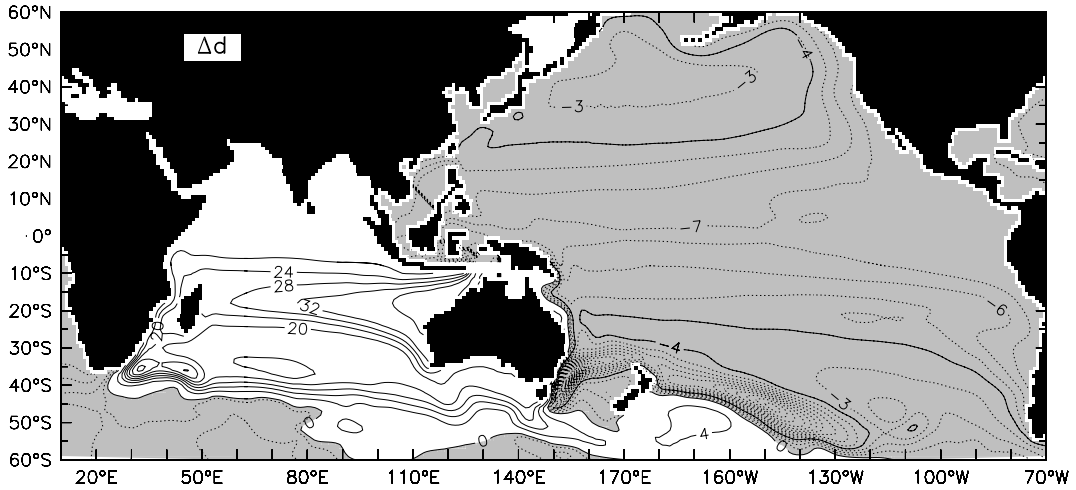


Fig. 17. Horizontal map of sea level  $\Delta d$  from Solution  $\Delta\text{COCO}$ . Contour intervals are 4 cm (solid) and 1 cm (dashed).

shift in the position of the ACC in Solution COCO, the anomalous currents interacting strongly with the shallow bottom topography. Transport changes are 14.2 and  $-1.3$  Sv in the Indian and Pacific sectors, respectively, from an ACC transport of 179.6 Sv in Solution COCO'.

Figs. 18b and 18c also plot velocity changes across the  $\rho_2$  and  $\rho_3$  density surfaces, respectively. Across-layer velocities for Solution COCO and COCO' are defined by

$$w_i = -\nabla \cdot \int_{z_b}^{z_i} (\mathbf{v} + \mathbf{v}^*) dz, \tag{4}$$

where  $z_b$  is the bottom depth,  $z_i$  is the depth of the  $\rho_i$  surface, and  $\mathbf{v}^*$  is the “bolus” velocity of the GM mixing scheme. The fields plotted in the two figures are  $\Delta w_2$  and  $\Delta w_3$ , respectively. The two fields are “noisier” than their counterparts in LOM (Figs. 12b and 12c), because COCO has additional sources of diffusion and because there are numerical errors in the evaluation of  $w_i$ . One error source is the interpolation needed to define  $z_i$  from density grid points, which can be inaccurate in regions of large vertical or horizontal density gradients. Another is the evaluation of  $\mathbf{v}^*$  itself, which is not an explicit model variable. As a result, the transfer of water between layers is often difficult to interpret.

Regions of upward transfer (upwelling) and downward transfer (downwelling) are broadly similar to those for LOM (Figs. 12b and 12c). There is downwelling in  $\Delta w_2$  in the southeastern Indian Ocean and south of Australia, and upwelling in  $\Delta w_2$  along the coasts of South and North America, and upwelling in the subpolar Pacific Ocean in both  $\Delta w_2$  and  $\Delta w_3$ . In the ACC region, there are small-scale patches of across-layer transfer in both  $\Delta w_2$  and  $\Delta w_3$  due to meandering currents in locations where the  $\rho_2$  and  $\rho_3$  surfaces outcrop. There is also a prominent, dipole-like feature in  $\Delta w_2$  in the central South Pacific (Fig. 18b), caused by the near-surface cyclonic circulation (Fig. 17): The stronger upwelling patch is generated when layer 3 water crosses the  $\rho_2$  outcrop line to enter layer 2, and the weaker downwelling patch is caused by the opposite change.

Other prominent regions of transfer are the bands of upwelling and downwelling along the east coasts of Australia and Africa in  $\Delta w_2$  and  $\Delta w_3$  and along the equator in the Pacific and Indian Oceans mostly in  $\Delta w_2$ . They are generated primarily by GM mixing, which decreases the large isopycnal slope across the boundary currents and has no counterpart in LOM. In principle, including  $\mathbf{v}^*$  in (4) should eliminate the influence of GM mixing on  $w_i$ . In fact, our estimate of  $\mathbf{v}^*$  is inaccurate due to the errors noted after (4), and in our solutions it only weakens the influence.

It is noteworthy that the coastal bands have opposite signs along Australia and Africa. In both Solutions COCO and COCO', the bands consist of a narrow region of upwelling adjacent to the coast and a broader region of downwelling offshore. Along Australia, the slope is smaller in Solution COCO than COCO' because the IT weakens the EAC; consequently, the upwelling and downwelling bands are weaker in Solution COCO,

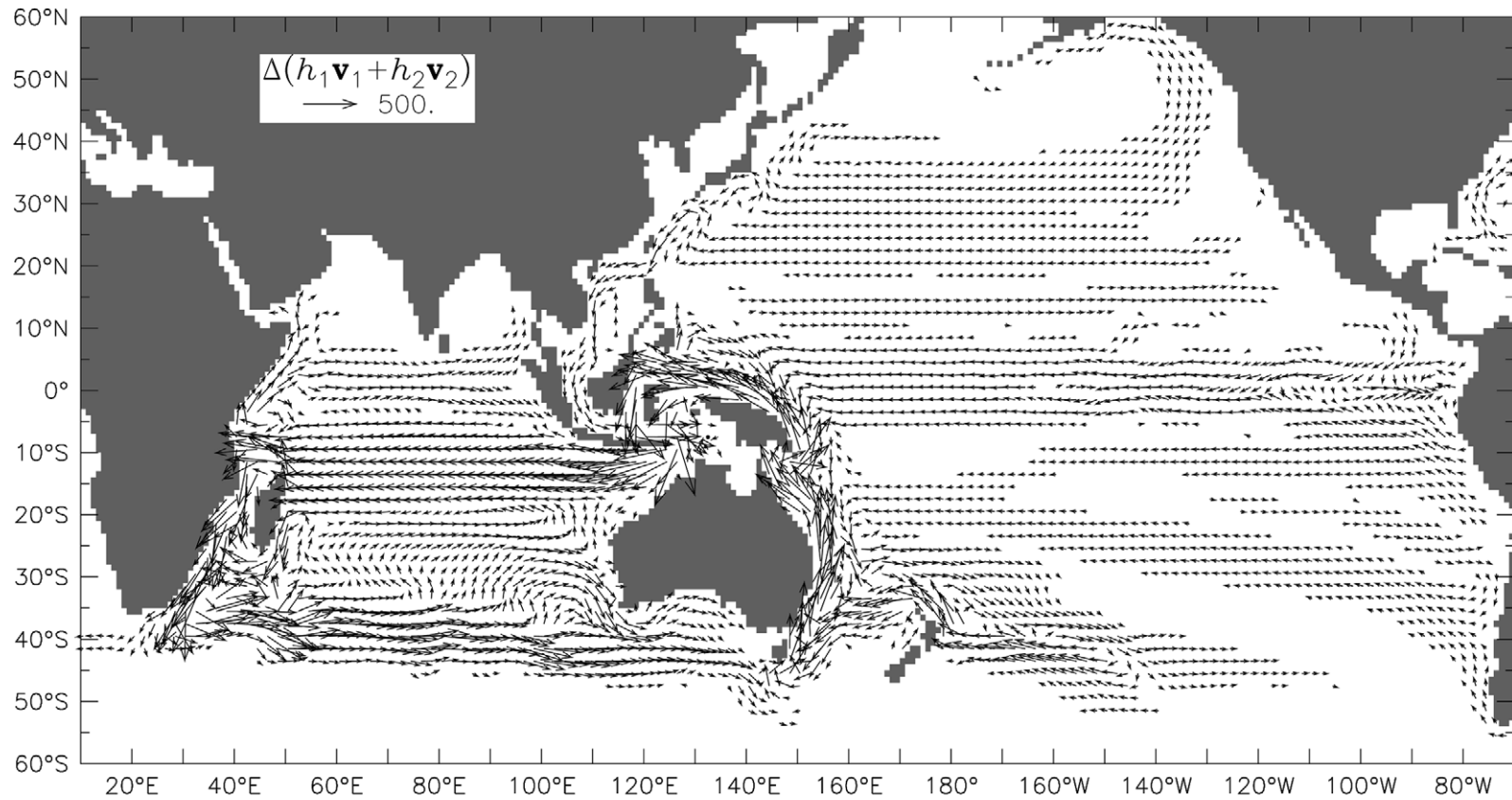


Fig. 18a. Horizontal map of transport/width vectors for layer 1 + 2 from Solution  $\Delta$ COCO. The layer is defined at the beginning of Section 5. To illustrate weaker flows better, arrow lengths are proportional to the square root of the vector amplitudes, so that the unit of the calibration arrow is  $(\text{cm}^2/\text{s})^{\frac{1}{2}}$ .

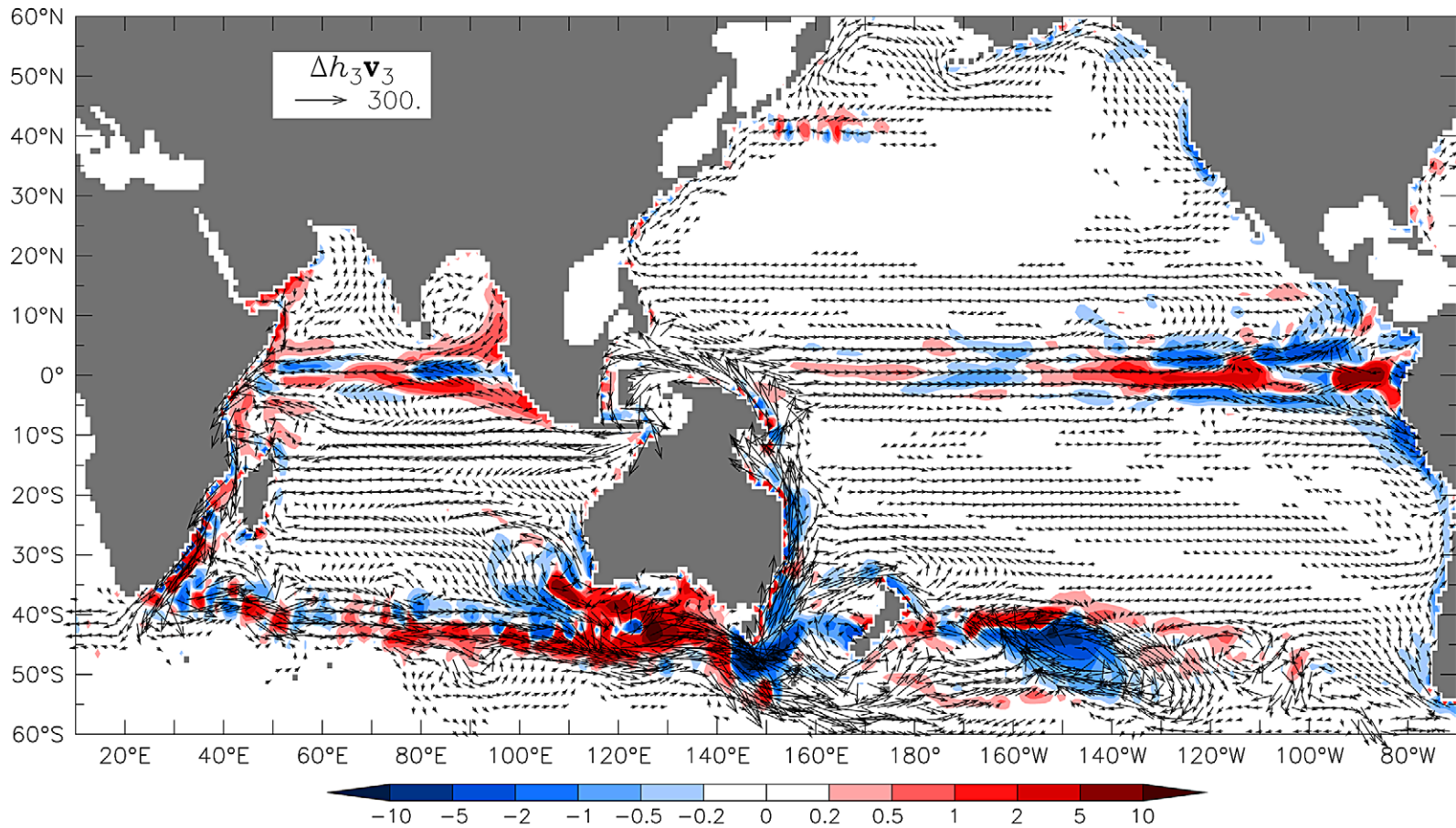


Fig. 18b. As in Fig. 18a, except for layer 3 defined at the beginning of Section 5. Also shown are across-interface velocity anomalies at the bottom of layer 2,  $\Delta w_2$ , with negative values indicating a transfer of water from layer 3 into layer 2. The unit for the color bar is  $10^{-4}$  cm/s.

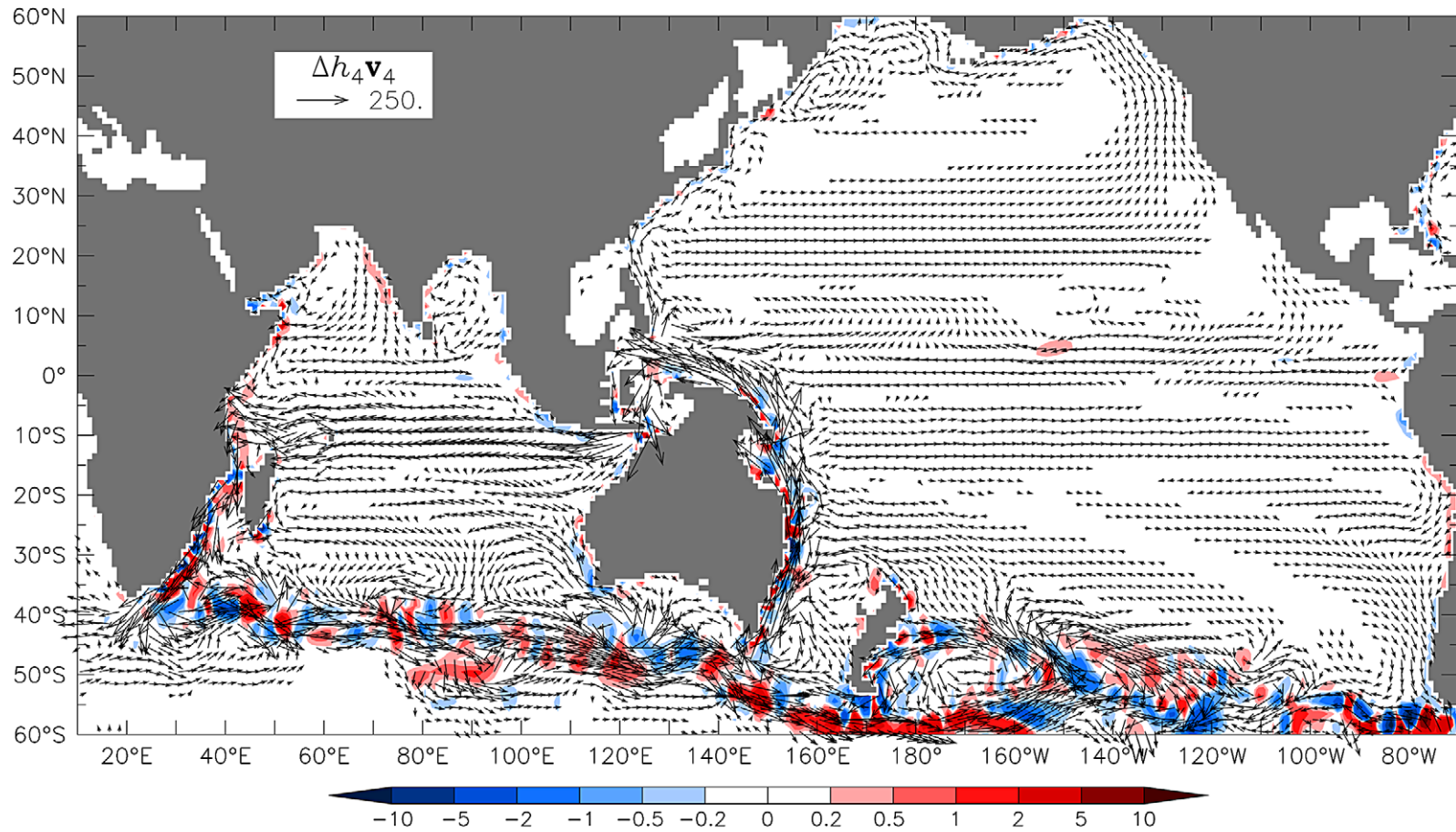


Fig. 18c. As in Fig. 18a, except for layer 4 defined at the beginning of Section 5. Also shown are across-interface velocity anomalies at the bottom of layer 3,  $\Delta w_3$ , with negative values indicating a transfer of water from layer 4 into layer 3. The unit for the color bar is  $10^{-4}$  cm/s.

and the near-shore and offshore bands are reversed in Solution  $\Delta\text{COCO}$ , appearing as bands of anomalous downwelling and upwelling, respectively (Fig. 18). Along Africa, the IT *strengthens* the poleward coastal current, and the change is in the opposite sense, that is, to intensify the across-layer transfers in Solution  $\text{COCO}'$ . Analogous arguments explain the change in sign of the equatorial bands between the two oceans.

5.2. Indonesian Seas

Fig. 19 plots the transport/depth profile of  $\Delta v$  integrated across the Indonesian passages (black curves in each panel). The total transport is 15.5 Sv, somewhat smaller than the value determined from the inviscid Island Rule (17 Sv), the decrease due to viscosity, bottom drag, the interaction of bottom topography with baroclinicity (the JEBAR effect), or other nonlinear effects (Wajsowicz, 1995; Godfrey, 1996). The transport is highly surface trapped, with 91% (9.6 Sv) of the total transport occurring above 400 m. In contrast to Solution  $\Delta\text{LOM}$  and the observations, the flow does not have a deep relative maximum, a consequence of  $\text{COCO}'$ 's coarse bottom topography lacking a throughflow passage below about 1000 m.

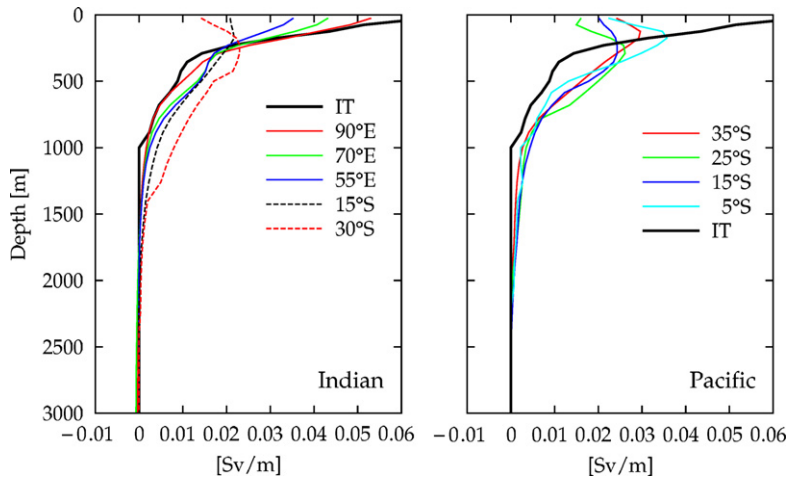


Fig. 19. Transport/depth profiles (Sv/m) for the currents that carry IT-associated transport in the Indian (left) and Pacific (right) Oceans from Solution  $\Delta\text{COCO}$ . The profiles are located across the Indonesian passages at 8.5°S (IT), across the Indian Ocean near 10°S (90°E, 70°E, and 50°E), along Africa (15°S and 40°S), and along the east coasts of Australia and New Guinea (30°S, 15°S, and 5°S). The profiles are all plotted as positive in the direction of the IT transport. The zonal transports across the Indian Ocean are determined by integrating the eastward flow from 15°S to 5°S. The western boundary transports are obtained almost everywhere by integrating the alongshore current from the coast,  $x_w(y, z)$ , to 6° offshore, in order to include the offshore reverse flow of the Munk layer. The exception is at 25°S, where the integration extends to  $x_w(10°S, z) + 6°$  in order to avoid distortions associated with the Coral Sea.

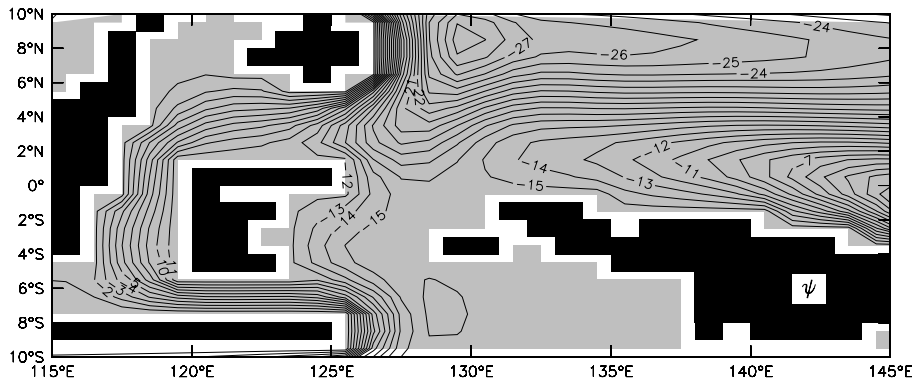


Fig. 20a. Horizontal map of the barotropic streamfunction  $\psi$  in the Indonesian Seas from Solution  $\text{COCO}$ . The contour interval is 1 Sv.

Circulations in the Indonesian Seas are similar to those in the LCS and LOM solutions, with sources for the shallow and deep IT cores coming from the northern and southern hemispheres, respectively (compare Fig. 20 with Figs. 8 and 13). In this case, inertial overshoot of the NGCC is clearly *not* the cause of layer 1 + 2 water coming from the north as all of it retroflects east of 130°E, because of the large horizontal viscosity in COCO (top panel of Fig. 20b). Instead, the northern source is ensured by the inertial overshoot of the Mindanao Current, some of which extends as far south as the equator before retroflecting into the NECC. One obvious difference among the solutions results from the absence of Halmahera Island in COCO: in the LCS and LOM solutions, the near-surface IT loops clockwise around Halmahera with northward flow along the northeast coast of Sulawesi, whereas in Solution COCO there is southward flow there. As in LOM, most of the layer 4 IT passes through the Banda Sea, rather than the Makassar Strait (bottom panel of Fig. 20b), in this case because the shallow bottom topography there blocks most of the layer 4 flow. In contrast to

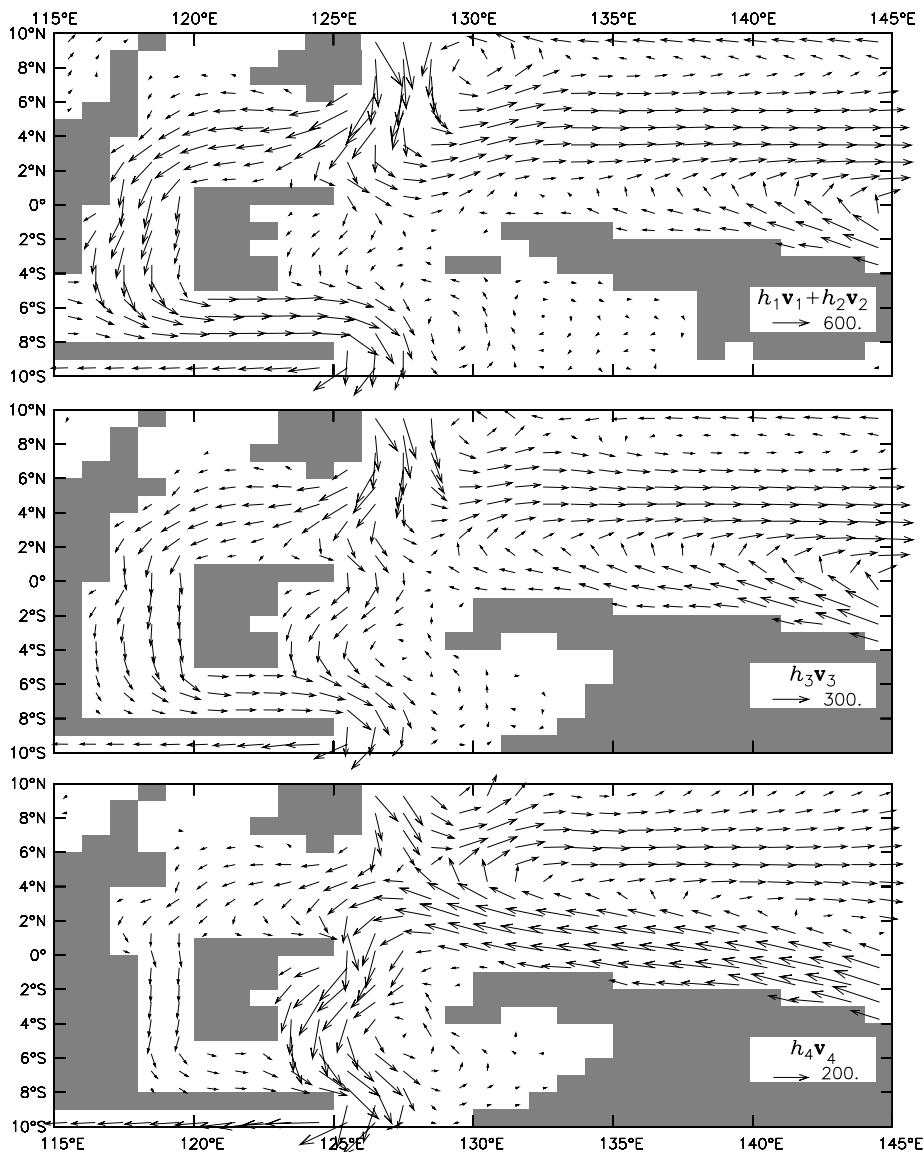


Fig. 20b. Horizontal maps of transport/width vectors in the Indonesian Seas for layer 1 + 2 (top), layer 3 (middle), and layer 4 (bottom) from Solution COCO. To illustrate weaker flows better, arrow lengths are proportional to the square root of the vector amplitudes, so that the unit of the calibration arrow is  $(\text{cm}^2/\text{s})^{\frac{1}{2}}$ .

LOM, the layer 3 flow is from the Pacific to Indian Ocean; its flow field resembles a combination of the layer 1 + 2 and layer 4 circulations, but with and northern hemisphere water still supplying most of the IT.

### 5.3. Indian Ocean

Similar to the LCS and LOM solutions,  $\Delta d$  indicates that there is a surface, geostrophic, westward jet across the basin near 10°S, southward flow in the interior ocean and along the African coast from 10°S to 17°S, and eastward return currents in the interior ocean from 17°S to 35°S and south of 40°S along the northern edge of the ACC (Fig. 17). These flows can also be seen in layer 1 + 2 (Fig. 18a), although they are distorted by the inclusion of subsurface (layer 2) currents. For example, there is westward flow in layer 1 + 2 just south of Madagascar, whereas eastward geostrophic flow is indicated by  $\Delta d$ ; this difference is caused by shear within layer 1 + 2, with weaker eastward flow in layer 1 overlying stronger westward flow in layer 2. In layers 3 and 4, there is northwestward flow extending from the southwest corner of Australia that compensates for the southeastward, shallower currents (Fig. 18b).

The narrowness of the southeastward, surface current in Fig. 17 is striking. A similar circulation exists in Solution  $\Delta$ LCS (Fig. 3), except that it is spread much more broadly across the interior ocean. The sharpness of the jet in COCO is likely due to nonlinearities, that alter the propagation direction of baroclinic Rossby waves (Rhines and Young, 1982; Luyten et al., 1983, LPS) allowing them to converge to form a front (Dewar, 1991, 1992). Hirst and Godfrey (1993) note a similar, and stronger, circulation in their difference solution, attributing it to localized convective overturning off Southwest Australia as well as to LPS-type dynamics. In COCO, there is localized downwelling (subduction) near Australia, which could help to narrow the jet; however, convection is not active there, likely because COCO includes GM mixing (Danabasoglu and McWilliams, 1995; England and Rahmstorf, 1999). Interestingly, the southeastward surface jet also exists in Solutions COCO and COCO', although it is much weaker in the latter. An eastward current in this latitude band also exists in the real ocean, the South Indian Countercurrent (SICC; Siedler et al., 2006; Palastanga et al., 2007). Currently, the dynamics of the SICC are not known. Our solutions and those of Hirst and Godfrey (1993) suggest that it is a significant branch of the IT-associated circulation.

As for the other solutions, the currents around the perimeter of the southern Indian Ocean in Solution  $\Delta$ COCO tend to become less surface trapped away from the Indonesian passages (Fig. 19), mostly due to divergences and convergences associated with the interior baroclinic flow rather than to diapycnal mixing. For example, note the marked near-surface weakening from 15°S to 30°S, which is caused by the shallow eastward current south of Madagascar.

### 5.4. Pacific Ocean

#### 5.4.1. South Pacific

In contrast to Solution  $\Delta$ LOM, circulations in the interior of the South Pacific in Solution  $\Delta$ COCO are not negligible. There are two, prominent circulations, one extending from the southern tip of South America and the other from the central South Pacific (Fig. 18). The South-American circulation represents a weaker flow of AAIW, with southeastward flow toward South America in layers 4 and 3 beneath northwestward flow in layer 1 + 2. As for the analogous situation in the Indian Ocean, a broader circulation is present in Solution  $\Delta$ LCS (Fig. 3), the narrower flow in Solution  $\Delta$ COCO attributable to LPS-type dynamics. As noted above, the circulation in the central South Pacific appears to be driven by a northward shift of the ACC in Solution COCO. There is considerable baroclinic shear associated with this circulation, as is evident from a comparison of Figs. 16 and 17. The cause of this shear is likely subduction across the  $\rho_2$  and  $\rho_3$  out-crop lines, but the direct connection of the circulation to downwelling regions is not obvious in Figs. 18b and 18c.

Fig. 19 illustrates the vertical structure of the South Pacific, western boundary currents in Solution  $\Delta$ COCO, plotting transport/depth profiles at 35°S, 25°S, 15°S, and 5°S. Similar to the other models, the flow that enters the Pacific basin extends to intermediate depths. Interestingly, from 35°S to 25°S the surface (sub-surface) current weakens (strengthens), owing to the aforementioned central-South Pacific overturning circulation. Farther north, the western boundary current becomes increasingly surface trapped, with marked

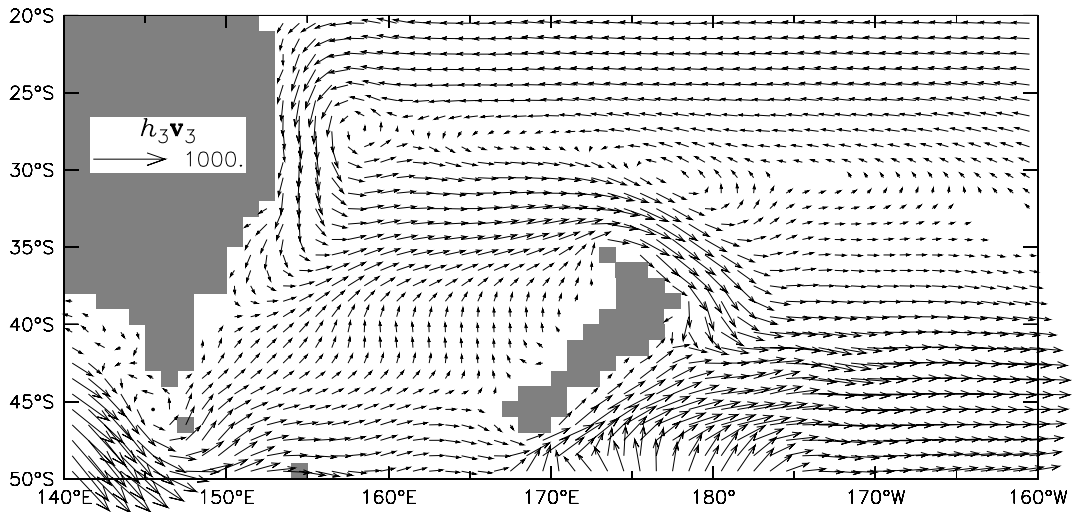


Fig. 21. Horizontal map of transport/width vectors in the Southwest Pacific for layer 3 from Solution COCO. To illustrate weaker flows better, arrow lengths are proportional to the square root of the vector amplitudes, so that the unit of the calibration arrow is  $(\text{cm}^2/\text{s})^{\frac{1}{2}}$ . The flow fields in layers 1 + 2 and 4 (not shown) are very similar.

shallowing occurring north of 15°S. The shallowing is more significant south of 5°S than it is in Solution  $\Delta\text{LOM}$  because of the South-American circulation, which is absent in Solution  $\Delta\text{LOM}$ .

Fig. 21 shows the layer 3 flow field from Solution COCO in the Southwest Pacific. Consistent with observations, there is no direct flow into the basin along the Australian coast, and water enters the South Pacific mostly in the eastern ocean. Similar to Solution LOM, some ACC water first enters the Pacific basin west of New Zealand, flowing northeastward across the interior of the Tasman Sea, and then eastward and southward around New Zealand to rejoin the northernmost part of the ACC. There are similar, but weaker, northward intrusions in layers 1 + 2 and 4, and the overall transport between New Zealand and Australia is northward (8 Sv).

Fig. 22 illustrates the effect of the IT on the SEC bifurcation latitude, showing sections of annual-mean, meridional transports/depth within 2° of the Australian coast from historical observations (top; Qu and Lindstrom, 2002) and within 6° of the Australian coast from Solutions COCO (middle) and COCO' (bottom). In each panel, the zero contour line defines the bifurcation latitude. In the observations, the bifurcation latitude is located just north of 16°S at the surface and near 22°S at 800 m, the depth of the AAIW core in the region. The bifurcation latitude in Solution COCO has a poleward shift with depth similar to the observations, varying from about 14°S at the surface to 19°S at 600 m, and it is shifted considerably southward with respect to the curve in Solution COCO'. As for LOM, the shift in position is caused almost entirely by the northward anomalous flow of the EAC in Solution  $\Delta\text{COCO}$ , rather than by a change in the interior circulation of the South Pacific, the deep shift being larger because the background EAC in Solution COCO' weakens with depth. The modeled shift, however, is not as large as the observed one. A possible reason for the discrepancy is that the EAC driven by the Pacific winds (in Solution COCO') is somewhat too strong at depth; this problem could result from diffusion in the interior Pacific being too strong, so that the SEC, which feeds the EAC, is itself too deep.

The Great Barrier Reef Undercurrent (GBRUC) flows northward along the northeast coast of Australia at depths below 200 m (top panel of Fig. 22). Since its discovery by Church and Boland (1983), the processes that drive the GBRUC are not clear. Our results suggest that the IT is its cause, through the large southward shift of the subsurface bifurcation latitude.

#### 5.4.2. Tropical Pacific

Consistent with the LCS and LOM solutions, there are generally westward, near-surface (layer 1 + 2) and eastward, subsurface (layer 3) flows across the basin in the tropical Pacific that are linked by upwelling in the

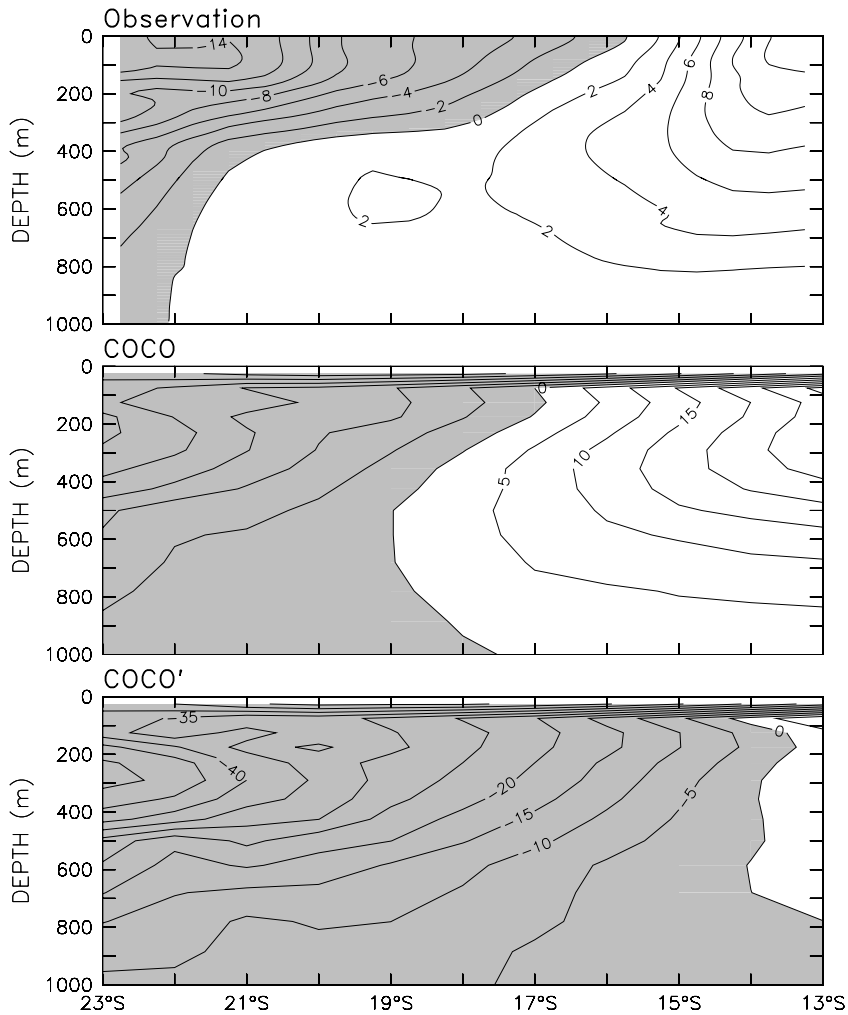


Fig. 22. Sections of alongshore transport/depth ( $10^{-3}$  Sv/m) from observations (top), Solution COCO (middle), and Solution COCO' (bottom). Observed values are derived from geostrophic velocities based on historical hydrographic data referenced to 1200 m (Qu and Lindstrom, 2002). Modeled values are obtained by integrating the alongshore current from the coast,  $x_{in}(y, z)$ , offshore to  $x_{in}(10^{\circ}\text{S}, z) + 6^{\circ}$ , in order to include the offshore reverse flow of the Munk layer and to avoid distortions caused by the Coral Sea. Positive values are northward, and the zero contour indicates the bifurcation of the SEC. Contour intervals are 2 cm in the top panel, and 5 cm in the middle and bottom panels.

far-eastern ocean, the area integral of  $\Delta w_2$  east of  $110^{\circ}\text{W}$  from  $20^{\circ}\text{S}$  to  $20^{\circ}\text{N}$  being  $+1.9$  Sv (Figs. 18a and 18b). An exception to this general pattern occurs east of  $110^{\circ}\text{W}$  where the equatorial differences are reversed. In both Solution COCO and COCO', there is a westward equatorial current in layer 3 in the eastern ocean, the model's Equatorial Intermediate Current (EIC), which appears to be generated by downwelling centered near  $90^{\circ}\text{W}$ . The vertical structures of the EUC and EIC are similar in both solutions but isopycnals are shallower in Solution COCO, with the top of layer 3 (the  $26.5 \sigma_{\theta}$  surface) lying at the bottom of the EUC in Solution COCO but lying in the middle of the EIC in Solution COCO'. As a consequence, in Solution COCO there is less (more) of the EIC in layer 1 + 2 (layer 3) and more downwelling into layer 3, accounting for the aforementioned reversals.

Solution  $\Delta\text{COCO}$  has eastward currents in layer 3 on either side of the equator across the Pacific, the model TJs (Fig. 18b). Consistent with the LOM solutions, the southern TJ is linked to upwelling off Peru (McCreary et al., 2002; Furue et al., 2007). In contrast, the northern TJ is linked to upwelling offshore from Central America and along Mexico, rather than the Costa Rica dome. [In fact, there are surface, anticlockwise and subsur-

face, clockwise circulations about the Costa Rica dome in Solution  $\Delta$ COCO, but they are shallow features contained in layer 1 + 2. It is not clear why they are so shallow; however, a deep (layer 3) recirculation is present in a solution with a higher resolution (Furue et al., 2007, to be submitted for publication), suggesting that COCO's coarse resolution may be one cause.] Note also that there is no flow from the Indian to Pacific Ocean in layer 3, possibly due to stronger diffusion in COCO. Finally, Solution  $\Delta$ COCO suggests that the source waters for both the northern and southern TJs are from the southern hemisphere. The situation is almost the same in Solution COCO, except that some water in the northern TJ may come from the Mindanao Current (middle panel of Fig. 20b).

Interestingly, the TJs still exist in Solution COCO' with essentially the same transport. This property suggests that the existence and strength of the TJs in COCO are determined largely by processes internal to the Pacific, rather than by the IT. Specifically, the TJs are one branch of an overturning cell in the South Pacific, similar to but somewhat larger and deeper than the Subtropical Cells. Nevertheless, the TJs are impacted by the IT, as their core occurs at a temperature that is  $1^\circ\text{C}$  warmer in Solution COCO than in COCO': without the IT, layer 1 + 2 is thicker, and hence water for the off-equatorial upwelling regions comes from somewhat warmer levels. Recall that the TJs in Solution LOM' vanished from layer 3, suggesting that the IT was required for their existence (McCreary et al., 2002). Based on our COCO results, a better interpretation is that the TJs still exist in Solution LOM' but they are located within layer 2; there, they are blended into the stronger thermocline circulation and so are impossible to detect, a limitation of LOM's low vertical resolution.

As for Solution LOM', the cross-equatorial exchange of intermediate water is weakened when the Indonesian passages are closed. In layer 3, water flows across the equator to nearly  $4^\circ\text{N}$  in Solution COCO (middle panel of Fig. 20b), whereas it flows only to the equator in Solution COCO' (not shown) and the Mindanao Current supplies all the water for the eastward interior currents north of the equator. Recall that in Solution LOM' northern hemisphere water flowed considerably farther south in layer 3 along the New Guinea coast (to  $9^\circ\text{S}$ ); the smaller change in Solution COCO' is likely due to its TJs not being as strongly linked to the IT as they are in LOM'. In layer 4, the northward flow along the New Guinea coast is much weaker in Solution COCO'. It does not cross the equator, but rather retroflects there to flow eastward just south of the equator, supporting the hypothesis that the IT is the reason that AAIW flows into the northern hemisphere.

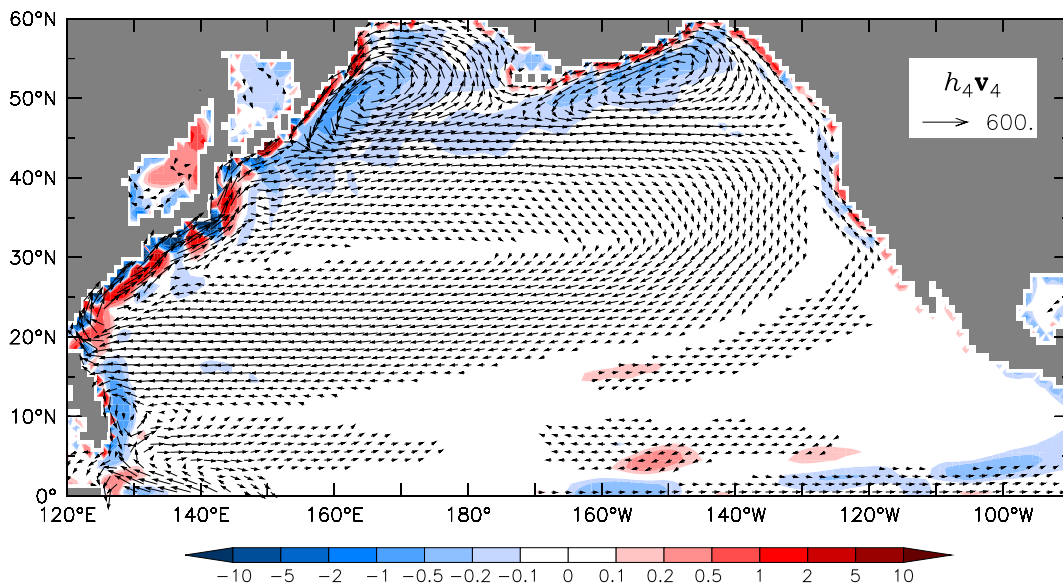


Fig. 23. Horizontal maps of transport/width vectors ( $\text{cm}^2/\text{s}$ ) in the North Pacific for layer 4 from Solution COCO. To illustrate weaker flows better, arrow lengths are proportional to the square root of the vector amplitudes, so that the unit of the calibration arrow is  $(\text{cm}^2/\text{s})^{1/2}$ . Also shown are across-interface velocities at the bottom of layer 3,  $w_3$ , with negative values indicating a transfer of water from layer 4 into layer 3. The unit for the color bar is  $10^{-4} \text{ cm/s}$ .

### 5.4.3. North Pacific

Similar to LOM, much of the layer 4 transport leaves the basin through the Indonesian passages (1.9 Sv out of 2.5 Sv; Fig. 18c), and the rest flows into the North Pacific (0.6 Sv at 10°N). By 25°N, the northward transport is reduced to 0.4 Sv, due to diffusion into shallower levels, and this transport eventually enters the sub-polar ocean. In Solution  $\Delta$ COCO, the primary pathway into the subpolar region is the far-eastern ocean (Fig. 18c). In Solution COCO, however, the window pathway is almost eliminated, with only a narrow coastal pathway remaining, and the major pathway is via the eastward current between the Subtropical and Subpolar Gyres (Fig. 23).

As in Solution LOM, there is no direct pathway for layer 4 water from the equator into the North Pacific along the western boundary in Solution COCO (Fig. 23). Water bends offshore in an eastward current about 5–10°N that extends to the dateline, with most of it bending northward in the interior ocean to join the westward-flowing branch of the STG. The layer 4 STG is much broader than it is in Solution LOM (Fig. 15), pointing toward a tighter linkage between layers 3 and 4 in COCO due to diffusion. There is no indication of any layer 4 currents due to Hawaii that were present in Solution LOM, owing to the HR winds being too smoothed to have regions of localized wind curl near Hawaii and to the lack of eddies.

## 6. Summary and discussion

In this paper, we investigate circulations in the Indian and Pacific Oceans associated with the IT, particularly concerning the circulation of subthermocline and upper-intermediate waters in the Pacific. We utilize a hierarchy of models: a linear, continuously stratified (LCS) model, a nonlinear,  $4\frac{1}{2}$ -layer model (LOM), and a global OGCM (COCO). Perhaps most importantly, the models differ markedly in their parameterizations of diffusion, and this property accounts for many of the differences in the baroclinic circulations of solutions. In the LCS model, diffusion is represented by second- or fourth-order vertical mixing that relaxes density toward its background state,  $\rho_b(z)$ . In LOM, diffusion is determined by the transfer of water between layers; it occurs primarily in regions where layer thicknesses become too thin or too thick, thereby concentrating diffusion in regions of upwelling and subduction (Appendix A). In COCO, isopycnal, horizontal, and thickness (GM) diffusion parameterizations are included throughout the basin, and there is vertical diffusion everywhere except in the upper tropical Pacific.

The opening of the Indonesian passages effectively provides a source (sink) of upper-layer fluid to the Indian (Pacific) Ocean, and all the models respond dynamically to this forcing by radiating waves away from the Indonesian passages (Section 3.1). The barotropic response rapidly adjusts to an equilibrium state in only a few months. The baroclinic adjustment is much more slow. In the LCS model, the minimum adjustment time for an individual baroclinic mode is the smaller of the time it takes a Rossby-wave to cross the Indian Ocean from the southern edge of Australia,  $T_n$ , and the damping time,  $t_n$ ; the minimum spin-up time for the complete system,  $T$ , is then the largest of the spin-up times for each mode. For reasonable parameter choices,  $T$  is of the order of 25–50 years. Timescale  $T$ , however, does not measure the spin-up time for all aspects of the adjustment: the adjustment time for the larger Pacific basin is considerably longer, as is the time for the advection of various water masses in COCO. Nevertheless, an adjustment time of 50 years or so does seem to hold for all three models.

Because the models share a common dynamics, basic features of solutions are the same. When the Indonesian passages are opened, there is a transfer of mass from the Pacific to Indian Ocean, raising sea level in the Indian Ocean and lowering it in the Pacific (Figs. 3, 11 and 17). The Indian Ocean rise is accompanied by a deepening of the thermocline, with the deepening in LOM, for example, being larger than 100 m off the west coast of Australia. The steady-state barotropic responses in the LCS difference solutions and Solution  $\Delta$ COCO consist primarily of an anticlockwise circulation in the southern Indian Ocean with meridional branches confined to the western boundaries of both oceans (Figs. 2 and 16); although LOM does not have a barotropic mode, a similar circulation dominates the total transport field of Solution  $\Delta$ LOM. In contrast, the steady-state baroclinic responses extend throughout the interiors of both oceans, a consequence of diffusion, which damps baroclinic waves and determines where water upwells and downwells (see the discussion of Fig. 2). In all the models, there tend to be southeastward, surface (northwestward, subsurface) baroclinic cur-

rents in the southern Indian Ocean, and westward and equatorward, surface (eastward and poleward, subsurface) currents in the Pacific (Figs. 3, 12 and 18). Details of the baroclinic circulations, however, differ considerably among the models because of their different diffusion parameterizations.

The IT is surface trapped in all the models (Figs. 6 and 19 and Table 2). In addition, there is a subsurface, transport minimum in the LCS and LOM solutions, allowing for a secondary deep core. The minimum is caused by eastward-flowing, thermocline (layer 2) and subthermocline (layer 3) currents primarily in the tropical Pacific, which drain water from the western ocean near the depth of the minimum. Indeed, depending on the strength and parameterization of vertical diffusion in the interior Pacific, the draining can be so strong that the IT reverses at depth to flow from the Indian to Pacific Ocean (Table 2; middle panel of Fig. 13). In contrast, there is no transport minimum or deep core in COCO, likely because the deep passages of the Indonesian Seas ( $z \gtrsim -1000$  m) are not adequately resolved.

For most solutions, the IT source waters come from the northern hemisphere for the shallow core and from the southern-hemisphere for the deep one. In the LCS model, the northern source exists because the North Pacific tropical gyre generates an anticlockwise circulation in the Sulawesi Sea that is strong enough to eliminate or reverse the westward flow in the Sulawesi Sea associated with the IT (Figs. 8 and 9). In LOM and COCO, it exists because of the nonlinear overshoot of the Mindanao Current past the southern tip of the Philippines and the retroflection of the NGCC. The exception is for the LCS solution driven by ERA15 winds for which the shallow core also comes primarily from the south, a result of the South Pacific tropical gyre extending into the Sulawesi Sea and, hence, weakening the anticlockwise circulation there (Fig. 10).

The depth structures of the IT-associated currents in the difference solutions deepen around the perimeter of the southern Indian Ocean from being primarily surface trapped in the Indonesian passages to extending to intermediate depths at the entrance to the South Pacific; conversely, they shallow to the north along the east coast of Australia (Figs. 5 and 19 and Table 2). These changes result from divergences and convergences caused by the interior baroclinic currents. In the LCS difference solutions, the changes are gradual south of 5°S, because the interior flows are broad (Fig. 3). In contrast, they are more abrupt in Solutions ΔLOM and ΔCOCO, due to baroclinic circulations arising in localized, upwelling and downwelling regions; for example, in both solutions there is anomalous downwelling from layer 2 into layer 3 in the southeastern Indian Ocean due to subduction, and southeastward (northwestward) currents extend from this region in layer 1 + 2 (layer 3) along pathways that appear to follow Rossby-wave characteristics (Figs. 12 and 18). In Solution ΔCOCO, there are two overturning circulations in the South Pacific: one originating in the southeastern ocean, similar but oppositely directed to the one in the Indian Ocean; and another in the central South Pacific due to a shift in the position of the ACC (Fig. 18). In all the models, the Pacific profiles shallow markedly north of 5°S, a consequence of the eastward interior flows (EUC and TJs) driven by near-equatorial upwelling.

In the difference solutions, IT-associated water enters the Pacific basin along the east coast of Australia, and most then flows directly to the Indonesian Seas along the western boundary. In solutions with open passages, however, the inflow occurs in the eastern South Pacific. In Solutions LOM and COCO, much of the inflow first enters the basin in the Tasman Sea, and then circulates around New Zealand to rejoin the ACC before entering the Pacific farther to the east (Figs. 14 and 21). This pathway does not appear to exist in reality (Ridgway, 2005, private communication), and it may be present in the solutions due to the models' inaccurate simulation of the ACC (e.g. Tilburg et al., 2001).

In all the models, the bifurcation latitude of the SEC shifts southward when the passages are opened, considerably more at depth than near the surface (Fig. 22; end of Section 4.4.1). The shift is caused almost entirely by the increased northward transport of the western boundary currents along Australia associated with the IT, rather than by changes in the interior circulation. Interestingly, the northward-flowing GBRUC owes its existence to the larger shift at depth and, hence, to the IT, as it is absent in the solutions with closed passages.

Solutions ΔLOM and ΔCOCO have eastward currents on either side of the equator in layer 3, representing strengthened TJs (Figs. 12b and 18b). The increase is caused by the draining of layer 1 + 2 water from the Pacific basin by the IT, which increases upwelling of layer 3 water into layer 2 in the eastern ocean. The structures of the southern TJs are similar in both models, extending across the basin to the South American coast.

On the other hand, the structures of the northern TJs are quite different, circulating around an upwelling region in the Costa Rica dome in Solution  $\Delta$ LOM and extending to upwelling regions along Central and North America in Solution  $\Delta$ COCO. The difference between the two models is traceable to the Costa Rica dome upwelling extending only into layer 2 in COCO, possibly due to its coarse resolution (Furue et al., 2007, to be submitted for publication).

In Solutions LOM and COCO, most of the layer 4 flow exits the Pacific basin via the IT, with much of the rest flowing into the subpolar region of the North Pacific. The pathways by which layer 4 water flows from the equator into the subpolar ocean are very different in the two models. In Solution LOM, the northward pathway of layer 4 water is disrupted by eddy-driven currents associated with instabilities of the HLCC (Figs. 12c and 15). Interestingly, the HLCC is driven entirely by orography-induced wind curl present in the ECMWF winds, since Hawaii is not included as a land mass in the basin. In Solution COCO, however, layer 4 water retroflects offshore from the western boundary at about 5–10°N to circulate around the perimeter of a broad, deep STG, with most of it bending northward to join the westward-flowing branch of the STG and the rest joining a narrow coastal current along North America (Fig. 23). There is no impact of Hawaii in COCO because it is forced by highly smoothed Hellerman and Rosenstein (1983) winds, for which the influence of Hawaii is weak.

In Solutions  $\Delta$ LOM and  $\Delta$ COCO, layer 4 water enters the SPG through a baroclinic “window” in the northeast corner of the basin (Figs. 12c and 18c). This deep, across-gyre exchange is driven by strengthened upwelling from layer 4 to layer 3 in the subpolar ocean, caused by the draining of shallower waters by the IT. In Solutions LOM and COCO, however, there are no window flows because the difference fields must be added to strong, double-gyre (STG and SPG) circulations for which the flow around their perimeter is everywhere southward. As a result, actual pathways of water parcels enter the SPG as they flow eastward across the basin between the two gyres (Figs. 15 and 23; Endoh et al., 2004).

When the Indonesian passages are closed in LOM (Solution LOM'), the layer 3 and layer 4 tropical circulations change significantly. In layer 3, upwelling along Peru north of 12°S is eliminated, and there are no TJs, in agreement with the McCreary and Lu (2001) result. In addition, layer 3 water from the northern hemisphere flows southward along the New Guinea coast, and then crosses the basin to supply some of the water for the Peruvian upwelling south of 12°S, so that northern hemisphere water fills the near-equatorial ocean in layer 3. In layer 4, all water in the South Pacific STG bends southward at the Australian coast; as a result, there is essentially no flow anywhere in the tropical ocean, and circulations in the northern and southern hemispheres remain separate. Changes are less pronounced in Solution COCO'. In layer 3, flow along New Guinea weakens but remains northward. In addition, the transport of the TJs remains about the same, although they do shift to a shallower level about 1 °C warmer. These properties suggest that the TJs in COCO are supplied mostly by a source internal to the Pacific, rather than by the IT, namely, a South Pacific overturning cell, somewhat broader and deeper than the Subtropical Cells, that is closed by subduction near South America or east of New Zealand. (Based on the lack of TJs in their solution without an IT (McCreary and Lu, 2001), concluded that the IT was necessary for the existence of TJs. Solution COCO' suggests that an alternate interpretation is that they were raised into layer 2.) In layer 4, there is still northward flow along the New Guinea coast but, in agreement with Solution LOM', it does not cross the equator. This result supports the idea that the IT is the reason that AAIW flows into the northern hemisphere.

In conclusion, we have investigated how IT-associated circulations interact with wind-driven circulations in the Indian and Pacific Oceans. Among other things, we find that the IT vertical structure is strongly influenced by subsurface, eastward currents in the tropical Pacific, which account for its surface trapping and its split into near-surface and deep cores. Conversely, the IT impacts interior flows by strengthening the SICC, generating the GBRUC, and either causing or increasing the flow of Pacific thermostat water and AAIW to the equator and into the northern hemisphere. More generally, the sensitivity of subsurface circulations in our solutions to the parameterization and strength of vertical mixing points toward the need for improving subsurface-mixing schemes in models. Finally, our research raises a number of dynamical issues, such as the specific processes that maintain the SICC and the impacts of local forcing and the South China Sea through-flow on circulations within the Indonesian Seas. We are planning to investigate these, and other related, issues in future studies.

## Acknowledgements

This study was supported by the National Science Foundation through Grant OCE00-95906 and by the Japan Agency for Marine-Earth Science and Technology (JAMSTEC) through its sponsorship of the International Pacific Research Center. We are grateful to Hideyuki Nakano, who kindly provided us with his code for COCO. Discussions with Billy Kessler, Ken Ridgway, Jim Potemra, Max Yaremchuk, and Zuojun Yu were very helpful. This manuscript is SOEST Contribution No. 7125 and IPRC Contribution No. 454.

## Appendix A. Diapycnal processes in LOM

The across-interface velocities in LOM are composed of three parts:

$$w_{ei} = \frac{(h_i - \mathcal{H}_e)^2}{\mathcal{H}_e t_e} \theta(\mathcal{H}_e - h_i), \quad (\text{A1a})$$

$$w_{di} = -\frac{(h_i - \mathcal{H}_d)^2}{\mathcal{H}_d t_d} \theta(h_i - \mathcal{H}_d) \theta[(y - y_{ni})(y - y_{si})], \quad (\text{A1b})$$

$$w_{mi} = \epsilon \left( \frac{1}{h_i} - \frac{\mathcal{H}_{i+1}}{\mathcal{H}_i} \frac{1}{h_{i+1}} \right), \quad (\text{A1c})$$

where  $h_i$  is the thickness of layer  $i$ ,  $\mathcal{H}_e = 40$  m,  $\mathcal{H}_d = 80$  m,  $\mathcal{H}_i$  is the initial thickness of layer  $i$  (see Section 2.2),  $t_e = 0.2$  days,  $t_d = 180$  days,  $\epsilon = 10^{-5}$  m<sup>2</sup>/s, and  $\theta$  is a step-function equal to 1 when its argument is positive and 0 otherwise; latitude pairs,  $(y_{ni}, y_{si})$ , are (18°N, 15°S), (37°N, 32°S), and (90°N, 45°S) for layers 1–3, respectively, except in the Indian Ocean where  $y_{ni} = 90^\circ\text{N}$  for all three layers. (With  $y_{ni} = 90^\circ\text{N}$ , there is no subduction in the northern hemisphere for layer  $i$ .) Velocity  $w_{ei}$  is active whenever  $h_i$  becomes thinner than  $\mathcal{H}_e$ ; it represents either entrainment into a surface mixed layer or the influx of mass into a thin subsurface layer where vertical shear is presumed large (McCreary et al., 2002). Velocity  $w_{di}$  is active in each layer poleward of the latitude pairs,  $(y_{ni}, y_{si})$ , and wherever  $h_i$  becomes thicker than  $\mathcal{H}_d$ ; it parameterizes subduction from the surface mixed layer at subtropical and higher latitudes. Note that the pairs shift poleward for the deeper layers; as a result, subduction extends to deeper layers at higher latitudes, as it does in the real ocean. Velocity  $w_{mi}$  tends to relax layer thicknesses back to their initial values, and so corresponds to vertical diffusion in the LCS model and COCO.

The across-interface velocities acting at the bottoms of layers 1–3 are then given by

$$w_1 = w_{e1} + w_{d1} + w_{m1} - w_{e2} \theta(h_1 - \mathcal{H}_e), \quad (\text{A2a})$$

$$w_2 = w_{e2} \theta(\mathcal{H}_e - h_1) + w_{d2} + w_{m2} - w_{e3} \theta(h_2 - \mathcal{H}_e), \quad (\text{A2b})$$

$$w_3 = w_{e3} \theta(\mathcal{H}_e - h_2) + w_{d3} + w_{m3}. \quad (\text{A2c})$$

Velocity  $w_4 = 0$ , so that no transfers are allowed across the base of layer 4 and the total mass of the system is conserved. According to the first terms on the right-hand sides of Eqs. (A2), when both  $h_1$  and  $h_2$  are less than  $\mathcal{H}_e$  the upper two layers behave as a single mixed layer of thickness  $h_1 + h_2$  with an entrainment rate  $w_{e2}$  at its base; similarly, when  $h_1$ ,  $h_2$ , and  $h_3$  are all less than  $\mathcal{H}_e$ , the top three layers behave like a single mixed layer with entrainment rate  $w_{e3}$ . Note also that when the layer overlying a thin layer is thicker than  $\mathcal{H}_e$ , as in the last terms of (A2a) and (A2b), water is detrained into the layer from above, a specification that is needed in order for the model to develop TJs (McCreary et al., 2002).

In the ACC region, northward Ekman drift cannot be balanced by southward geostrophic flow since the region lacks meridional boundaries. Given the  $w_i$  velocities specified above, this process thins the upper three layers to  $\mathcal{H}_e$  and then drains all water from layer 4 south of the southern tip of South America, a situation that the model cannot handle. To avoid this problem, wind stress  $\tau$  is multiplied by a factor  $\delta$  that equals 1 when  $h_4 > \mathcal{H}_a = 200$  m, 0 when  $h_4 < 100$  m, and varies linearly in between. Thus, the model is unforced when  $h_4 < 100$  m; in that case, the four active layers in effect have zero thickness (outcrop), so that all forcing is transferred to the deep ocean. It is noteworthy that this scheme does not allow for a deep overturning cell,

in which water from the deep ocean is entrained into layer 4 across the ACC boundary and is balanced by outflow elsewhere (such as in the North Atlantic in a global model); this lack may be one reason why the ACC is located too far north in LOM (Section 4.1).

The preceding scheme results in a sharp front in the  $h_i$  fields at the northern edge of the ACC region. To smooth this front, Laplacian mixing on  $h_i$  is included with the coefficient,

$$\kappa_h = \kappa_{h0} \left[ (1 - \delta) + 10 \frac{\delta \mathcal{H} - h_i}{\delta \mathcal{H}} \theta(\delta \mathcal{H} - h_i) \right] \theta(\mathcal{H}_a - h_4), \quad (\text{A3})$$

where  $\kappa_{h0} = 3 \times 10^7 \text{ cm}^2/\text{s}$  and  $\delta \mathcal{H} = 15 \text{ m}$ . According to (A3), mixing occurs only when  $h_4 < \mathcal{H}_a$  and strengthens considerably if layers become thinner than 15 m. Note that these definitions of  $\delta$  and  $\kappa_h$  are not spatially limited. In practice, however,  $\delta \neq 1$  and  $\kappa_h \neq 0$  only in the ACC region, since only there does  $h_4$  ever become less than 200 m.

## References

- Bryan, K., 1984. Accelerating the convergence to equilibrium of ocean–climate models. *Journal of Physical Oceanography* 14, 666–673.
- Cessi, P., Bryan, K., Zhang, R., 2004. Global seiching of thermocline waters between the Atlantic and the Indian-Pacific Ocean Basins. *Geophysical Research Letters* 31, L04302. doi:10.1029/2003GL01909.
- Church, J.A., Boland, F.M., 1983. A permanent undercurrent adjacent to the Great Barrier Reef. *Journal of Physical Oceanography* 13, 1747–1749.
- Danabasoglu, G., McWilliams, J.C., 1995. Sensitivity of the global ocean circulation to parameterizations of mesoscale tracer transports. *Journal of Climate* 8, 2967–2987.
- da Silva, A., Young, C.C., Levitus, S., 1994. Atlas of Surface Marine Data 1994, vol. 1: Algorithms and Procedures. NOAA Atlas NESDIS 6. US Department of Commerce, NOAA, NESDIS, Washington, DC, 83 pp.
- Dewar, W.K., 1991. Arrested fronts. *Journal of Marine Research* 49, 21–52.
- Dewar, W.K., 1992. Spontaneous shocks. *Journal of Physical Oceanography* 22, 505–522.
- Endoh, T., Mitsudera, H., Xie, S.-P., Qiu, B., 2004. Thermohaline structure in the subarctic North Pacific simulated in a general circulation model. *Journal of Physical Oceanography* 34, 360–371.
- England, M.H., Rahmstorf, S., 1999. Sensitivity of ventilation rates and radiocarbon uptake to subgrid-scale mixing. *Journal of Physical Oceanography* 29, 2802–2827.
- Ffield, A.L., Vranes, K., Gordon, A.L., Susanto, R.D., Garzoli, S.L., 2000. Temperature variability within Makassar Strait. *Geophysical Research Letters* 27, 237–240.
- Fine, R., Lukas, R., Bingham, F.M., Warner, M.J., Gammon, R.H., 1994. The western equatorial Pacific is a water mass crossroads. *Journal of Geophysical Research* 99, 25063–25080.
- Flament, P., Kennan, S., Lumpkin, C., Sawyer, M., Stroup, E., 1998. The ocean. In: Juvik, S.P., Juvik, J.O. (Eds.), *Atlas of Hawaii*, Third ed., pp. 82–86.
- Furue, R., McCreary Jr., J.P., Yu, Z., Wang, D., 2007. Dynamics of the southern Tsuchiya Jet. *Journal of Physical Oceanography* 37, 531–553.
- Furue, R., McCreary Jr., J.P., Yu, Z., to be submitted for publication. Dynamics of the northern Tsuchiya Jet.
- Gent, P.R., McWilliams, J.C., 1990. Isopycnal mixing in ocean circulation models. *Journal of Physical Oceanography* 20, 150–155.
- Gibson, J.K., Kålberg, P., Uppala, S., Hernandez, A., Nomura, A., Serrano, E., 1999. ERA-15 Description (Version 2 – May 1999). ECMWF Re-Analysis Project Series 1, European Centre for Medium-Range Weather Forecasts, 84 pp.
- Godfrey, J.S., 1989. A Sverdrup model of the depth-integrated flow for the World Ocean allowing for island circulations. *Geophysical and Astrophysical Fluid Dynamics* 45, 89–112.
- Godfrey, J.S., 1996. The effects of the Indonesian Throughflow on ocean circulation and heat exchange with the atmosphere: a review. *Journal of Geophysical Research* 101, 12217–12237.
- Godfrey, J.S., Weaver, A.J., 1991. Is the Leeuwin Current driven by Pacific heating and winds? *Progress in Oceanography* 23, 300–328.
- Godfrey, J.S., Hirst, A.C., Wilkin, J.L., 1993. Why does the Indonesian Throughflow appear to originate from the North Pacific? *Journal of Physical Oceanography* 23, 1088–1098.
- Gordon, A.L., 1986. Inter-ocean exchange of thermocline waters. *Journal of Geophysical Research* 91 (suppl.), 5037–5046.
- Gordon, A.L., 2005. Oceanography of the Indonesian Seas and their throughflow. *Oceanography* 18, 14–27.
- Gordon, A.L., Fine, R., 1996. Pathways of water between the Pacific and Indian Oceans in the Indonesian Seas. *Nature* 379, 146–149.
- Gordon, A.L., Susanto, R.D., Field, A.L., 1999. Throughflow within Makassar Strait. *Geophysical Research Letters* 26, 3325–3328.
- Haney, R.L., 1971. Surface thermal boundary condition for ocean circulation models. *Journal of Physical Oceanography* 1, 241–248.
- Hellerman, S., Rosenstein, M., 1983. Normal monthly wind stress over the world ocean with error estimates. *Journal of Physical Oceanography* 13, 1093–1104.
- Hirst, A.C., Godfrey, J.S., 1993. The role of Indonesian Throughflow in a global ocean GCM. *Journal of Physical Oceanography* 23, 1057–1086.

- Hirst, A.C., Godfrey, J.S., 1994. The response to a sudden change in the Indonesian Throughflow in a global ocean GCM. *Journal of Physical Oceanography* 24, 1894–1910.
- Huang, R.-X., Cane, M.A., Naik, N., Goodman, P., 2000. Global adjustment of the thermocline in response to deepwater formation. *Geophysical Research Letters* 27, 759–762.
- Hu, D., Cui, M., Qu, T., Li, Y., 1991. A subsurface northward current off Mindanao identified by dynamic calculation. In: Takano, K. (Ed.), *Elsevier Oceanography of Asian Marginal Seas*, Oceanography Series, vol. 54. Elsevier, pp. 359–365.
- Hughes, T., Weaver, A.J., Godfrey, J.S., 1992. Thermohaline forcing of the Indian Ocean by the Pacific Ocean. *Deep-Sea Research* 39, 965–996.
- Johnson, H.L., Marshall, D.P., 2004. Global teleconnections of meridional overturning circulation anomalies. *Journal of Physical Oceanography* 34, 1702–1722.
- Lebedev, K.V., Yaremchuk, M.I., 2000. A diagnostic study of the Indonesian Throughflow. *Journal of Geophysical Research* 105, 11243–11258.
- Lee, T., Fukumori, I., Menemenlis, D., Xing, Z., Fu, L.-L., 2002. Effects of the Indonesian Throughflow on the Pacific and Indian Oceans. *Journal of Physical Oceanography* 32, 1404–1429.
- Leonard, B.P., 1979. A stable and accurate convective modelling procedure based on quadratic upstream interpolation. *Computer Methods in Applied Mechanics and Engineering* 19, 59–98.
- Leonard, B.P., MacVean, M.K., Lock, A.P., 1993. Positivity-preserving numerical schemes for multidimensional advection. NASA Technical Memorandum 106055, ICOMP-93-05.
- Leonard, B.P., MacVean, M.K., Lock, A.P., 1994. The flux-integral method for multidimensional convection and diffusion. NASA Technical Memorandum 106679, ICOMP-94-13.
- Levitus, S., 1994. *World Ocean Atlas 1994*, vol. 13. National Oceanographic Data Center, CD-ROM, <http://www.nodc.noaa.gov/>.
- Lindstrom, E., Lukas, R., Fine, R., Firing, E., Godfrey, S.J., Meyers, G., Tsuchiya, M., 1987. The western equatorial Pacific Ocean circulation study. *Nature* 330, 533–537.
- Lindstrom, E., Butt, J., Lukas, R., Godfrey, S.J., 1990. The flow through Vitiaz Strait and St. George's Channel, Papua New Guinea. In: Pratt, L. (Ed.), *The Physical Oceanography of Sea Straits*. Kluwer Academic, pp. 171–189.
- Lu, P., McCreary Jr., J.P., Klinger, B.A., 1998. Meridional circulation cells and sources of the Pacific Equatorial Undercurrent. *Journal of Physical Oceanography* 28, 62–84.
- Luyten, J.R., Pedlosky, J., Stommel, H., 1983. The ventilated thermocline. *Journal of Physical Oceanography* 13, 292–309.
- Masumoto, Y., Sasaki, H., Kagimoto, T., Komori, N., Ishida, A., Sasai, Y., Miyama, T., Motoi, T., Mitsudera, H., Takahashi, K., Sakuma, H., Yamagata, T., 2004. A fifty-year eddy-resolving simulation of the world ocean: preliminary outcomes of OFES (OGCM for the Earth Simulator). *Journal of the Earth Simulator* 1, 35–56.
- McCartney, M.S., 1977. Subantarctic mode water. In: Angel, M. (Ed.), *A Voyage of Discovery George Deacon 70th Anniversary Volume*. Pergamon Press, Oxford, pp. 103–119.
- McCartney, M.S., 1982. The subtropical recirculation of Mode Water. *Journal of Marine Research* 40 (suppl.), 427–464.
- McCreary Jr., J.P., 1981. A linear stratified ocean model of the Equatorial Undercurrent. *Philosophical Transactions of the Royal Society of London* 298A, 603–635.
- McCreary Jr., J.P., 1985. Modeling equatorial ocean circulation. *Annual Review of Fluid Mechanics* 17, 359–409.
- McCreary Jr., J.P., Kundu, P.K., 1987. On the dynamics of the throughflow from the Pacific into the Indian Ocean. *Journal of Physical Oceanography* 16, 2191–2198.
- McCreary Jr., J.P., Lu, P., 2001. Influence of the Indonesian Throughflow on the circulation of Pacific Intermediate Water. *Journal of Physical Oceanography* 31, 932–942.
- McCreary Jr., J.P., Han, W., Shankar, D., Shetye, S.R., 1996. Dynamics of the East India Coastal Current: Part 2. Numerical solutions. *Journal of Geophysical Research* 101, 13993–14010.
- McCreary Jr., J.P., Lu, P., Yu, Z., 2002. Dynamics of the Pacific Subsurface Countercurrents. *Journal of Physical Oceanography* 32, 2379–2404.
- Meyers, G., Baily, R.J., Worby, A.P., 1995. Geostrophic transport of the Indonesian Throughflow. *Deep-Sea Research I* 42, 1163–1174.
- Miyama, T., Awaji, T., Akitomo, K., Imasoto, N., 1995. Study of seasonal transport variations in the Indonesian seas. *Journal of Geophysical Research* 100, 20517–20541.
- Molcard, R., Fieux, M., Ilahude, A.G., 1996. The Indo-Pacific throughflow in the Timor Passage. *Journal of Geophysical Research* 101, 12411–12420.
- Murtugudde, R., Busalacchi, A.J., Beauchamp, J., 1998. Seasonal-to-interannual effects of the Indonesian Throughflow on the tropical Indo-Pacific basin. *Journal of Geophysical Research* 103, 21425–21440.
- Nakano, H., 2000. Modeling global abyssal circulation by incorporating bottom boundary layer parameterization. Ph.D. Thesis, University of Tokyo, 110 pp. (available from the Center for Climate System Research, University of Tokyo, 5-1-5 Kashiwanoha, Kashiwa-shi, Chiba 277-8568, Japan).
- Nakano, H., Suginohara, N., 2002a. Effects of bottom boundary layer parameterization on reproducing deep and bottom waters in a world ocean model. *Journal of Physical Oceanography* 32, 1209–1227.
- Nakano, H., Suginohara, N., 2002b. Importance of the eastern Indian for the abyssal Pacific. *Journal of Geophysical Research* 107, 3219–3232.
- National Geophysical Data Center, 1988. *Digital Relief of the Surface of the Earth*. Data Announcement 88-MGG-02, National Oceanic and Atmospheric Administration (NOAA), Boulder, Colorado.

- Palastanga, V., van Leeuwen, P.J., Schouten, M.W., de Ruijter, W.P.M., 2007. Flow structure and variability in the subtropical Indian Ocean: instability of the South Indian Ocean Countercurrent. *Journal of Geophysical Research* 112, C01001. doi:10.1029/2005JC00339.
- Pedlosky, J., 1984. Cross-gyre ventilation of the subtropical gyre: an internal mode in the ventilated thermocline. *Journal of Physical Oceanography* 14, 1172–1178.
- Potemra, J.T., 1999. Seasonal variations of upper ocean transport from the Pacific to the Indian Ocean via Indonesian straits. *Journal of Physical Oceanography* 29, 2930–2944.
- Qiu, B., Koh, D., Lumpkin, C., Flament, P., 1997. Existence and formation mechanism of the North Hawaiian Ridge Current. *Journal of Physical Oceanography* 27, 431–444.
- Qu, T., Lindstrom, E.J., 2002. A climatological interpretation of the circulation in the western South Pacific. *Journal of Physical Oceanography* 32, 2492–2508.
- Qu, T., Lindstrom, E.J., 2004. Intrusion of Antarctic Intermediate Water in the western Pacific. *Journal of Physical Oceanography* 34, 2104–2118.
- Qu, T., Mitsudera, H., Yamagata, T., 1998. On the western boundary current in the Philippine Sea. *Journal of Geophysical Research* 103, 7537–7548.
- Qu, T., Mitsudera, H., Yamagata, T., 1999. A climatology of the circulation and water mass distribution near the Philippine coast. *Journal of Physical Oceanography* 29, 1488–1505.
- Reid, J.L., 1965. Intermediate waters of the Pacific Ocean. *Johns Hopkins Oceanographic Studies*, vol. 2. Johns Hopkins University Press, Baltimore, Maryland, 85 pp.
- Reid, J.L., 1997. On the total geostrophic circulation of the Pacific Ocean: flow patterns, traces and transports. *Progress in Oceanography* 39, 263–325.
- Rhines, P.B., Young, W.R., 1982. A theory of the wind-driven circulation. I: Mid-ocean gyre. *Journal of Marine Research* 40 (suppl.), 559–596.
- Rochford, D.J., 1960. The intermediate depth waters of the Tasman and Coral Seas. I: The 27.20  $\sigma_\theta$  surface. *Australian Journal of Marine and Freshwater Research* 11, 127–147.
- Rodgers, K.B., Cane, M.A., Naik, N.H., 1999. The role of the Indonesian Throughflow in equatorial Pacific thermocline ventilation. *Journal of Geophysical Research* 104, 20551–20570.
- Roemmich, D., Cornuelle, B., 1992. The subtropical mode waters of the South Pacific Ocean. *Journal of Physical Oceanography* 22, 1178–1187.
- Row, L.R., Hastings, D.A., Dunbar, P.K., 1995. *TerrainBase Worldwide Digital Terrain Data Documentation Manual*. National Geophysical Data Center, Boulder, Colorado.
- Schiller, A., Godfrey, J.S., McIntosh, P.C., Meyers, G., Wijffels, S.E., 1998. Seasonal near-surface dynamics and thermodynamics of the Indian Ocean and Indonesian Throughflow in a general ocean circulation model. *Journal of Physical Oceanography* 28, 2288–2312.
- Schneider, N., 1998. Indonesian Throughflow and the global climate system. *Journal of Climate* 11, 676–689.
- Shriver, J.F., Hurlburt, H.E., 1997. The contribution of the global thermohaline circulation to the Pacific to Indian Ocean throughflow via Indonesia. *Journal of Geophysical Research* 102, 5491–5511.
- Siedler, G., Rouault, M., Lutjeharms, J.R.E., 2006. Structure and origin of the subtropical South Indian Ocean Countercurrent. *Geophysical Research Letters* 33, L24609. doi:10.1029/2006GL02739.
- Spall, M.A., 2000. Buoyancy-forced circulations around islands and ridges. *Journal of Marine Research* 58, 957–982.
- Susanto, R.D., Gordon, A.L., 2005. Velocity and transport of the Makassar Strait throughflow. *Journal of Geophysical Research* 110, C01005. doi:10.1029/2004JC00242.
- Talley, L.D., 1996. Antarctic Intermediate Water in the South Atlantic. In: Wefer, G. et al. (Eds.), *The South Atlantic: Present and Past Circulation*. Springer, New York, pp. 219–238.
- Talley, L.D., 1999. Some aspects of ocean heat transport by the shallow intermediate and deep overturning circulation. In: Clark, P., Webb, R., Keigwin, L. (Eds.), *Mechanisms of Global Climate Change at Millennial Time Scales*, Geophysical Monograph Series, vol. 112. American Geophysical Union, pp. 1–22.
- Talley, L.D., Sprintall, J., 2005. Deep expression of the Indonesian Throughflow: Indonesian Intermediate Water in the South Equatorial Current. *Journal of Geophysical Research* 110, C10009. doi:10.1029/2004JC00282.
- Tilburg, C.E., Hurlburt, H.E., O'Brien, J.J., Shriver, J.F., 2001. The dynamics of the East Australian Current System: The Tasman Front, the East Auckland Current, and the East Cape Current. *Journal of Physical Oceanography* 12, 2917–2943.
- Toggweiler, J.R., Dixon, K., Broecker, W.S., 1991. The Peru upwelling and the ventilation of the South Pacific thermocline. *Journal of Geophysical Research* 96, 20467–20497.
- Tsuchiya, M., 1975. Subsurface countercurrents in the eastern equatorial Pacific Ocean. *Journal of Marine Research* 33 (Suppl.), 145–175.
- Tsuchiya, M., 1991. Flow path of Antarctic Intermediate Water in the western equatorial South Pacific Ocean. *Deep-Sea Research* 38 (Suppl. 1), 272–279.
- Verschell, M.A., Kindle, J.C., O'Brien, J.J., 1995. Effects of Indo-Pacific throughflow on the upper tropical Pacific and Indian Oceans. *Journal of Geophysical Research* 100, 18409–18420.
- Vranes, K., Gordon, A.L., Field, A., 2002. The heat transport of the Indonesian Throughflow and implications for the Indian Ocean heat budget. *Deep-Sea Research II* 49, 1391–1410.
- Wajsowicz, R., 1993. The circulation of the depth-integrated flow around an island with application to the Indonesian Throughflow. *Journal of Physical Oceanography* 23, 1470–1484.

- Wajsowicz, R., 1995. The response of the Indo-Pacific throughflow to interannual variations in the Pacific wind stress. Part I: Idealized geometry and variations. *Journal of Physical Oceanography* 25, 1805–1826.
- Wyrski, K., 1961. *Physical Oceanography of Southeast Asian Waters*. NAGA Report 2, Scripps Institute of Oceanography, La Jolla, 195 pp.
- Xie, S.-P., Liu, W.T., Liu, Q., Nonaka, M., 2001. Far-reaching effects of the Hawaiian Islands on the Pacific Ocean – atmosphere system. *Science* 292, 1953–2204.
- Yu, Z., Maximenko, N., Xie, S.-P., Nonaka, M., 2003. On the termination of the Hawaiian Lee Countercurrent. *Geophysical Research Letters* 30, 1215. doi:10.1029/2002GL01671.
- Zenk, W., Siedler, G., Ishida, A., Holfort, J., Kashino, Y., Kuroda, Y., Miyama, T., Müller, T.J., 2005. Pathways and variability of the Antarctic Intermediate Water in the western equatorial Pacific Ocean. *Progress in Oceanography* 67, 245–281.